

A tool for mapping microglial morphology, morphOMICs, reveals brain-region and sex-dependent phenotypes

Received: 6 January 2022

Accepted: 16 August 2022

Published online: 30 September 2022

 Check for updates

Gloria Colombo ^{1,9}, Ryan John A. Cubero ^{1,9}, Lida Kanari ²,
Alessandro Venturino ¹, Rouven Schulz ¹, Martina Scolamiero³,
Jens Agerberg³, Hansruedi Mathys^{4,5,6,8}, Li-Huei Tsai ^{4,5,6},
Wojciech Chachólski³, Kathryn Hess⁷ and Sandra Siegert ¹ ✉

Environmental cues influence the highly dynamic morphology of microglia. Strategies to characterize these changes usually involve user-selected morphometric features, which preclude the identification of a spectrum of context-dependent morphological phenotypes. Here we develop MorphOMICs, a topological data analysis approach, which enables semiautomatic mapping of microglial morphology into an atlas of cue-dependent phenotypes and overcomes feature-selection biases and biological variability. We extract spatially heterogeneous and sexually dimorphic morphological phenotypes for seven adult mouse brain regions. This sex-specific phenotype declines with maturation but increases over the disease trajectories in two neurodegeneration mouse models, with females showing a faster morphological shift in affected brain regions. Remarkably, microglia morphologies reflect an adaptation upon repeated exposure to ketamine anesthesia and do not recover to control morphologies. Finally, we demonstrate that both long primary processes and short terminal processes provide distinct insights to morphological phenotypes. MorphOMICs opens a new perspective to characterize microglial morphology.

Morphological characterization of neuronal shapes has provided important insights into the diversity of cell types related to their genetic and functional features¹. Numerous studies have tried to apply a similar morphological analysis on microglia^{2–4}. Although they have revealed microglial heterogeneity^{5–7}, no study has established a high-throughput, minimally biased and consistent way to capture context-specific and sex-dependent changes in microglial

morphology during development and degeneration. Detecting subtle changes in the microglial morphology along the spectrum would offer an early readout of their immediate responses to local environmental cues⁶, as microglia are sensitive to changes in neuronal activity^{8–10}. Moreover, the majority of these analyses rely on restricted microglia sample sizes underestimating their full morphological spectrum.

¹Institute of Science and Technology Austria (ISTA), Klosterneuburg, Austria. ²Blue Brain Project, École Polytechnique Fédérale de Lausanne (EPFL), Geneva, Switzerland. ³Department of Mathematics, KTH Royal Institute of Technology, Stockholm, Sweden. ⁴Picower Institute for Learning and Memory, Massachusetts Institute of Technology, Cambridge, MA, USA. ⁵Department of Brain and Cognitive Sciences, Massachusetts Institute of Technology, Cambridge, MA, USA. ⁶Broad Institute of Harvard and MIT, Cambridge, MA, USA. ⁷Laboratory for Topology and Neuroscience, Brain Mind Institute, École Polytechnique Fédérale de Lausanne (EPFL), Lausanne, Switzerland. ⁸Present address: University of Pittsburgh Brain Institute and Department of Neurobiology, University of Pittsburgh School of Medicine, Pittsburgh, PA, USA. ⁹These authors contributed equally: Gloria Colombo, Ryan John A. Cubero. ✉e-mail: ssiegert@ist.ac.at

The microglia morphological phenotype is commonly determined with user-selected features from a three-dimensional (3D) reconstructed branching tree: these features can include total process length, branch number or number of terminal points. These scalar morphometric descriptors are then statistically compared across conditions. The drawback of this approach is the number and the type of selected features, which biases the biological readout: while too few selected features underrepresent a phenotypic difference, too many cause overfitting and introduce noise¹¹. Moreover, in contrast to neuronal morphological trees that are static on the gross structure, microglia processes are highly dynamic^{12,13} as they constantly survey their local environment¹². This introduces considerable intrinsic variability within the traced microglia population of a defined condition as well as the risk of selection bias to the extreme phenotypes. Establishing a reliable brain-region-specific morphological phenotype is critical for characterizing baseline morphology and tracking changes as deviations from the baseline.

To capture morphological phenotypes, complex morphological trees must be simplified with minimal information loss and retain as many features as possible. Applied topology provides new strategies for solving this problem, as it focuses on the shape properties of geometric objects without the need of morphometrics^{14,15}. In particular, the topological morphology descriptor (TMD), which assigns a barcode to any 3D tree, has been successfully applied for classification of cortical neuron morphologies¹⁴. When we first applied the TMD to ~10,000 3D-traced microglia across the rostrocaudal axis of seven selected adult brain regions, these data indicated a regional phenotype, but the diversity of the individual microglia obscured any well-defined separation.

Here, we developed our MorphOMICs pipeline to overcome the major limitations of feature-selection-based analysis and biological data variability. MorphOMICs combines TMD with bootstrapping, dimensionality reduction and data visualization techniques, enabling minimally biased identification of the baseline phenotype. When we applied this strategy, we found that the morphologies of adult microglia vary between brain regions and are different between sexes. This microglial sexual dimorphism gradually diminished along postnatal development. In contrast, the sex-specific phenotype diverged during neurodegenerative disease progression, where females differ in their context-dependent response from males. When we aligned the trajectories of development and degeneration, we obtained for each brain region a morphological spectrum that we used as a reference atlas to map novel conditions. Remarkably, we resolved morphological changes after repeated exposure to the anesthetic cocktail ketamine–xylazine–acepromazine (KXA) and revealed that microglial morphology reverts away from the control during the recovery process. Our method unravels a spectrum of microglial phenotypes and overcomes the classical dichotomized view of either surveilling or reactive microglia. Thus, MorphOMICs lays out an avenue toward a multimodal definition of the microglia state.

Results

MorphOMICs uncovers adult microglial heterogeneity

To address how morphological phenotypes differ between microglia across brain regions, we immunostained the adult C57BL/6J mouse brain with the allograft inflammatory factor 1 (Aif1/Iba1)¹⁶ for both sexes with at least biological triplicates. Then, we traced 9,997 cells and generated a library of 3D microglial skeletons from seven brain regions chosen to span the rostrocaudal axis with a preference for regions that are known to be affected in Alzheimer disease^{17–23}: the olfactory bulb (OB_{mg}), frontal cortex (FC_{mg}), dentate gyrus of the hippocampus (DG_{mg}), primary somatosensory cortex (S1_{mg}), substantia nigra (SN_{mg}), cochlear nucleus (CN_{mg}) and cerebellum (CB_{mg}; Fig. 1a). When we utilized morphometrics that are commonly used in the field of microglial morphology^{2,24,25}, we found non-significant differences across these brain regions with the exception of CB_{mg} and CN_{mg} (Extended Data Fig. 1a and Supplementary Table 1). We therefore applied the TMD^{14,15} for which each 3D skeleton was represented as a rooted tree with the microglial soma in the center, processes (edges), branching points (nodes) and process terminals (terminal points; Fig. 1b, i). The TMD converts the tree as a persistence barcode, where each bar represents the persistent process lifetime in terms of the radial distance from the soma (Fig. 1b)^{11,14}. Every bar is then collapsed into a single point in the persistence diagram summarizing the process's lifetime, which is then converted into a persistence image using Gaussian kernels²⁶ (Fig. 1b). The branching complexity is spatially represented by process length proportional to the distance from the diagonal (Fig. 1b). An example of this conversion with a representative microglial morphology is shown in Extended Data Fig. 1b. To quantify the differences between microglial morphologies across brain regions, we computed the pairwise TMD distance between the average persistence images¹⁴. While average persistence images did not differ strongly (Fig. 1c), hierarchical clustering suggested groups with FC_{mg}, OB_{mg}, and SN_{mg}, and S1_{mg} and DG_{mg} with CN_{mg} and CB_{mg} segregated (Extended Data Fig. 1c). When we looked at the individual persistence images, we found a wide variance between the individual microglia within a brain region, which made it challenging to distinguish regional phenotypes (Extended Data Fig. 1d). We note that this dispersion is not driven by an animal-based batch effect (Extended Data Fig. 1e).

To overcome this intrinsic variability within a microglial population, we developed MorphOMICs, which combines TMD with subsampling of persistence images, dimensionality reduction and data visualization strategies. Bootstrapping randomly draws, without replacement, a user-defined number of unique persistence images (x) from a microglial population pool (n) and iteratively generates bootstrapped persistence images (Fig. 1d). To display these bootstrapped persistence images for each brain region, we applied the nonlinear dimensionality reduction technique uniform manifold approximation and projection (UMAP; Fig. 1e), which converts the high-dimensional persistence images into a reduced two-dimensional

Fig. 1 | MorphOMICs dissects microglial morphology in adult healthy brains.

a, Sagittal view of the mouse brain (image from Allen Institute) with annotated brain regions. Confocal images of immunostained microglia (Iba1, green) and cell nuclei (Hoechst, blue) from adult C57BL/6J mice with zoom-in view. Scale bars, 50 μ m. **b**, Schematic of MorphOMICs pipeline covering the TMD with a mock microglia skeleton and plots. Red, longest process with start (#) and end (*). Each traced microglia was converted into a rooted tree (i), followed by a persistence barcode (ii), a persistence diagram (iii) and a persistence image (iv) with grayscale process density in 2D space. Blue spot, soma location. Arrow 1 indicates the distance from the soma. Arrow 2 indicates the length of processes, which increases with distance from the diagonal. Each persistence image (n) is summarized to an average persistence image of a condition. **c**, Average persistence images of the seven analyzed brain regions organized by hierarchical clustering (Extended Data Fig. 1b). Top-right corner: representative traced microglia. The darker the green, the higher the frequency distribution

of the processes. **d**, Schematic of MorphOMICs pipeline covering bootstrapping.

Left: microglial population (n) contains individual persistence images.

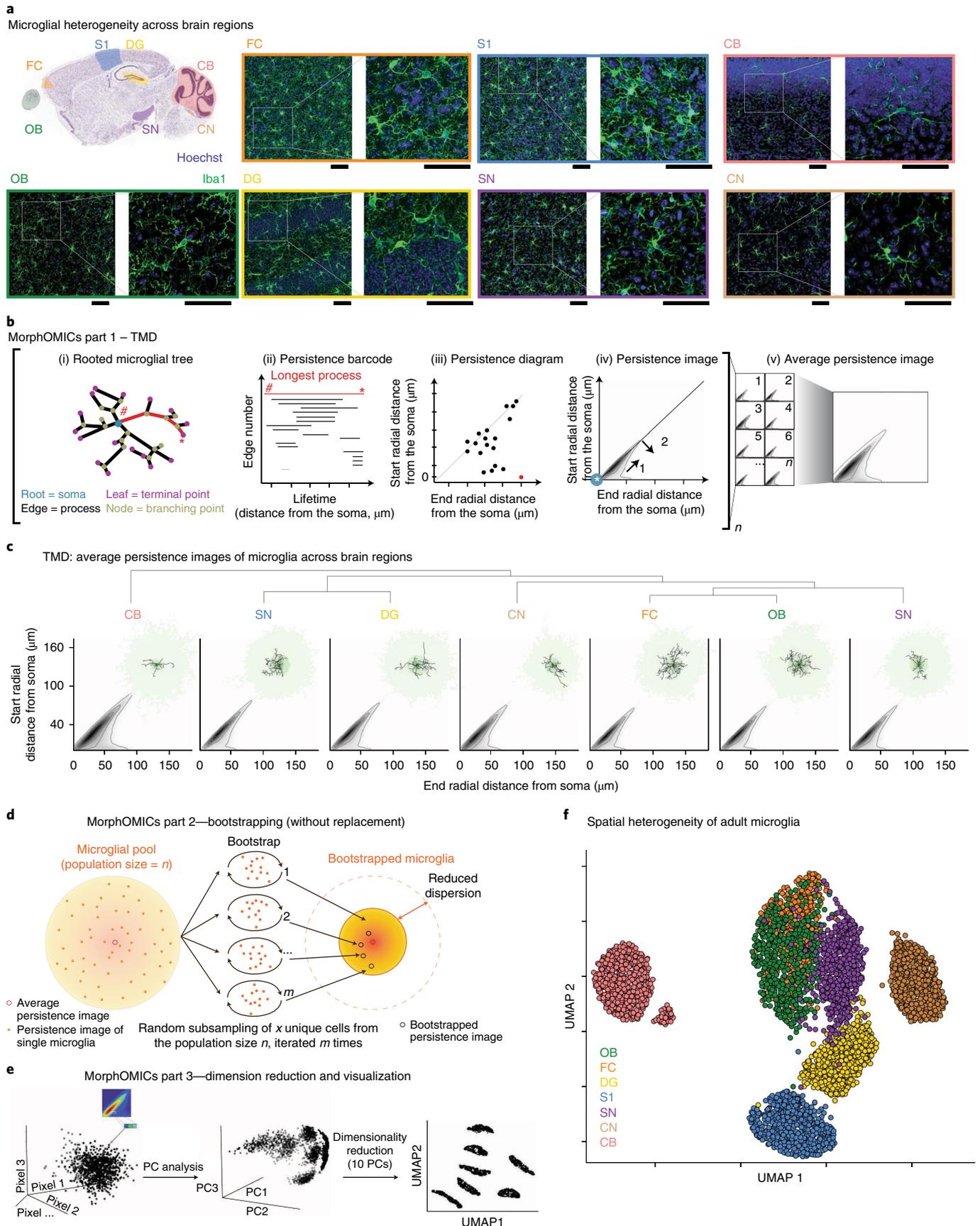
Center: average persistence image; x unique persistence images were drawn from each of n microglial pools to generate a bootstrapped persistence image. Right: repeating this process m times forms the bootstrapped pool.

e, Schematic of MorphOMICs pipeline covering dimension reduction and data visualization with UMAP. Left: each persistence image is pixelated; each pixel represents a dimension. Middle: reducing dimensions with principal component (PC) analysis. Right: further dimensionality reduction based on the first ten PCs. **f**, UMAP plot of MorphOMICs-analyzed adult microglia, color-coded for each brain region. Each dot represents a bootstrapped persistence image.

$n_{\text{samples}} = 500$ per condition ('Average and bootstrapped persistence images'). In **d**, see Supplementary Table 5 for the number of animals. Points situated close in the UMAP space indicate similar bootstrapped persistence image; however, the point's actual position is irrelevant.

(2D) representation preserving their global structure. While local distances are presumably better preserved in UMAP compared to *t*-distributed stochastic neighbor embedding (*t*-SNE)²⁷, the point's

actual position in the reduced space is irrelevant. After controlling for the bootstrapped-to-microglial population pool size ratio (Extended Data Fig. 2a–e and Supplementary Information), we applied



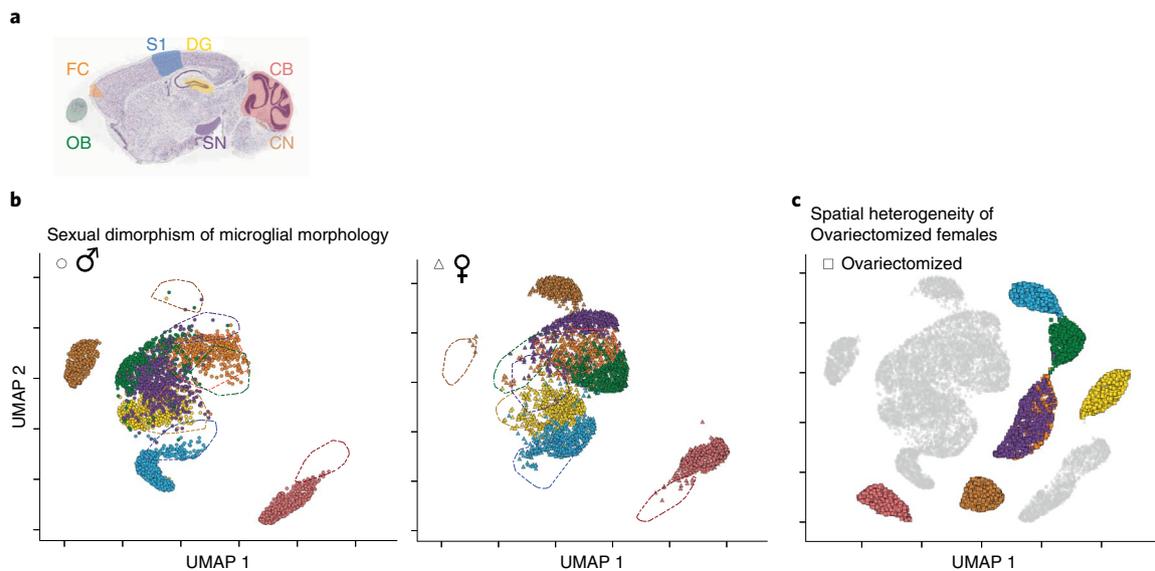


Fig. 2 | MorphOMICs identifies sexually dimorphic microglial morphology in healthy adults. **a**, Sagittal view of analyzed brain regions. **b,c**, MorphOMICs-analyzed microglia in male, female and ovariectomized adult mice. **b**, UMAP plot for each brain region color coded for males (left) or females (right) with

dashed lines as reference. Each dot represents a bootstrapped persistence image. **c**, UMAP plot of ovariectomized females. Ovariectomized brain regions are highlighted. Gray indicates the non-ovariectomized counterpart as reference. $n_{\text{samples}} = 500$ per condition ('Average and bootstrapped persistence images').

MorphOMICs to our 3D-microglia library. The UMAP plot exhibited a spatial separation similar to that of the hierarchical clustering of the average persistence images (Fig. 1c), with CB_{mg} separated from the other brain regions and FC_{mg} , OB_{mg} and SN_{mg} occupying a well-defined area in the UMAP space (Fig. 1f). However, MorphOMICs further revealed that OB_{mg} and FC_{mg} are intermingled, while DG_{mg} and $S1_{\text{mg}}$ formed distinct clusters. Importantly, these cluster segregations were stable even if we changed UMAP's hyperparameters (Extended Data Fig. 2f) or when we applied *t*-SNE visualization instead (Extended Data Fig. 2g). Finally, we also confirmed with stable ranks that the persistence barcodes maintained the region-specific phenotypes (Extended Data Fig. 2h). When we applied a support vector machine (SVM) algorithm to the stable ranks, the resulting classification accuracy confirmed the separation between brain regions in the UMAP space (Extended Data Fig. 3a). Notably, while the position of CN_{mg} varies with the choice of hyperparameters, its relative position to the other brain regions, especially DG_{mg} and SN_{mg} , remains consistent. Thus, we suspect that more complex morphological relationships between brain regions can exist as exhibited by CN_{mg} .

An alternative morphological simplification that is commonly performed in the microglia literature is Sholl analysis, which calculates the number of processes that intersect concentric spheres centered on the soma with a user-defined radius²⁸. When we applied Sholl analysis, we could not recapitulate the spatial segregation captured by MorphOMICs (Extended Data Fig. 3b). Even if we applied bootstrapping to Sholl curves, we could only dissect the regional heterogeneity for CB_{mg} and CN_{mg} (Extended Data Fig. 3c). Moreover, these clusters merged with increasing Sholl radius step size. Overall, these data indicate that adult brain regions have well-defined microglia morphological phenotypes, which MorphOMICs reliably uncovers.

Region-dependent, sexually dimorphic microglial phenotype

Next, we were interested in the extent of microglial sexual dimorphism across brain regions, which is only partially understood^{29,30}. We applied MorphOMICs to our library, and compared males and females within the UMAP space (Fig. 2a,b). As before, each brain region occupied a unique cluster in the plot, where CB_{mg} and CN_{mg} were most divergent. Strikingly, most brain regions separated female and male microglia,

with CB_{mg} , CN_{mg} , OB_{mg} , SN_{mg} and $S1_{\text{mg}}$ forming close but spatially separated clusters. In contrast, σ/DG_{mg} and FC_{mg} highly overlapped, suggesting rather minor morphological differences between the sexes. Interestingly, compared to Fig. 1c, the FC_{mg} and OB_{mg} cluster broke up: σFC_{mg} and σOB_{mg} formed spatially separated clusters, whereas $\text{♀}FC_{\text{mg}}$ and $\text{♀}OB_{\text{mg}}$ were intermingled. These morphological differences could depend on the microglia density. When we determined the number of microglia for each brain region and sex, we found that only CN_{mg} and OB_{mg} showed a significant sexual dimorphism (Extended Data Fig. 4a,b), which is also reflected in the strongest separation within the UMAP space (Fig. 2b). In contrast, microglia density does not explain the sexually dimorphic signature in CB_{mg} and SN_{mg} suggesting that density does not fully capture the dimorphic phenotype.

To determine whether these sex-specific phenotypic differences are hormone dependent, we expanded our library to include microglia from adult female mice that we ovariectomized at postnatal day (P) 20 (♀_{ov} ; Extended Data Fig. 4c) before they start the estrous cycle and enter puberty³¹. We found that the $\text{♀}_{\text{ov}}FC_{\text{mg}}$ cluster no longer intermingled with $\text{♀}_{\text{ov}}OB_{\text{mg}}$ in ovariectomized females but instead fused with $\text{♀}_{\text{ov}}SN_{\text{mg}}$ (Fig. 2c). This is surprising, as in non-ovariectomized mice, $\text{♀}SN_{\text{mg}}$ was close to but distinct from the intermingled $\text{♀}FC_{\text{mg}}$ and $\text{♀}OB_{\text{mg}}$ cluster. When we compared non-ovariectomized to ovariectomized females, we found that in the UMAP space ovariectomized females formed distinct clusters, spatially separated from their non-ovariectomized counterparts and did not resemble any hints of masculinization (Fig. 2b,c). These results demonstrate the existence of a brain-region-specific, sexually dimorphic phenotype, and that interfering with estrogen production before puberty affects microglial heterogeneity in adulthood.

Sexual dimorphism during development

Microglia originate in the yolk sac and infiltrate the nervous system early during embryonic development³². After microglia occupy a brain region, their morphology gradually becomes more branched during postnatal neuronal circuit refinement (Fig. 3a)^{33,34}. To determine whether microglial heterogeneity and the dimorphic phenotype already exist within the first postnatal weeks and before the onset of puberty, we sampled microglia from all seven brain regions at P7, P15 and P22 and included them in our library (Extended Data Fig. 5a,b).

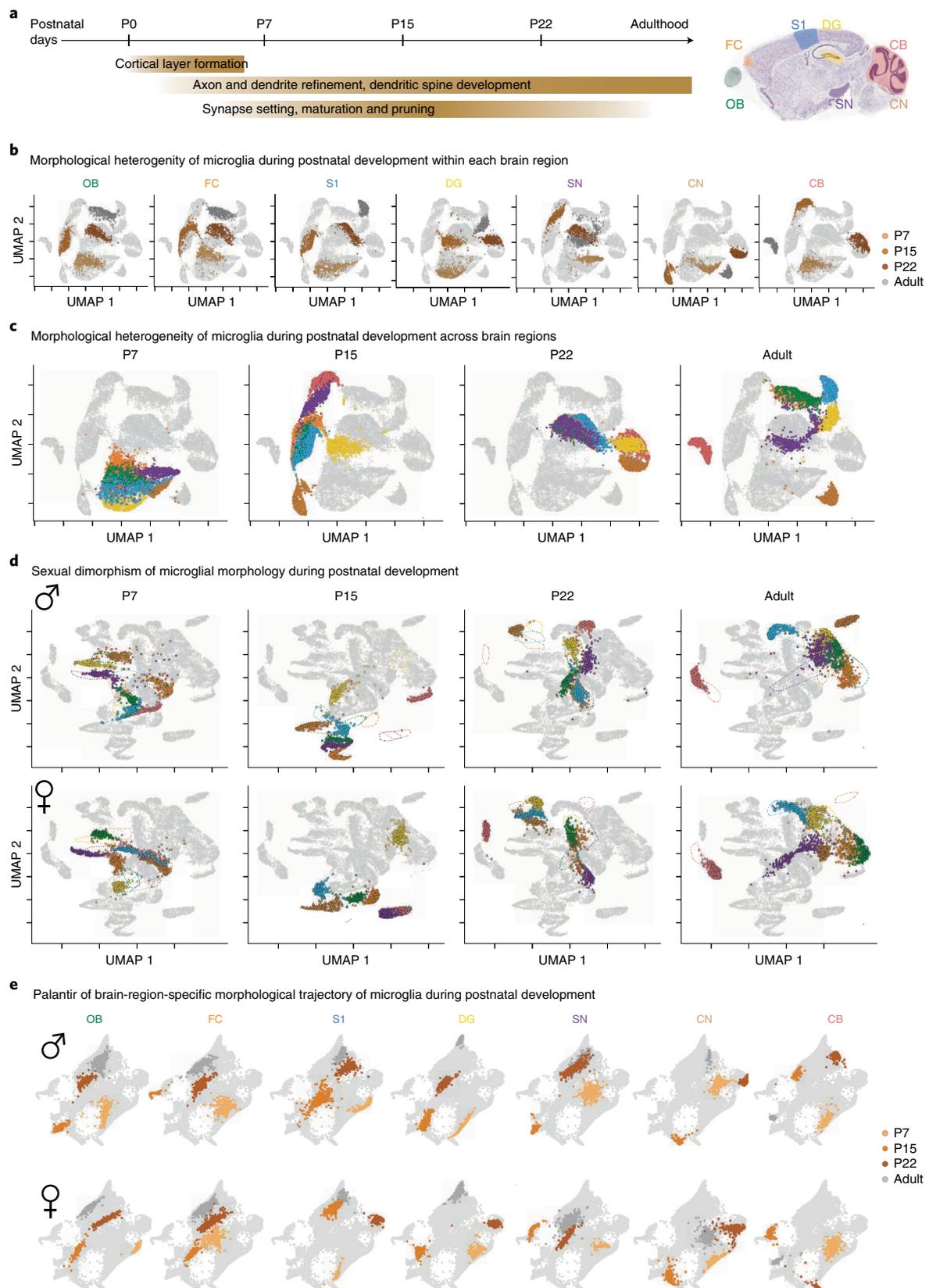


Fig. 3 | Microglial phenotypes during postnatal development. **a**, Timeline of postnatal brain development with highlighted events. Sagittal view of analyzed brain regions. **b–d**, UMAP plots of MorphOMICs-analyzed microglia across seven brain regions in *Cx3cr1-GFP^{+/+}* mice at P7, P15, P22 and adults (**b**), and color-coded brain regions for both sexes (**c**) and for each sex independently with dashed lines

as the reference for each developmental time point (**d**). **e**, Palantir reconstruction of microglia morphological trajectory from **d** with P7, P15, P22 and adults highlighted for each brain region. Nearby points indicate similar persistence images. Each dot represents a bootstrapped persistence image. $n_{\text{samples}} = 500$ per condition ('Average and bootstrapped persistence images').

Then, we applied MorphOMiCs and highlighted in the UMAP plots either each brain region (Fig. 3b) or the developmental time point (Fig. 3c). In all seven brain regions, no postnatal time points overlapped with the adult microglia (Fig. 3b), reflecting their morphological heterogeneity during development. When we analyzed each developmental time point individually, we found that at P7, all brain regions are distinct but occupy the same cluster, which shifted to a different cluster at P15 (Fig. 3c). Interestingly, CN_{mg} and DG_{mg} segregated and remained distinct from the other brain regions at P15 and P22, with CB_{mg} joining them at P22. Between P22 and adulthood, the clusters diverged to their adult microglial heterogeneity.

Next, we investigated whether sexual dimorphism affects the microglial phenotypic spectrum during development. To do this, we applied MorphOMiCs to males and females separately (Fig. 3d and Extended Data Fig. 5c). Surprisingly, we found that the clusters shown in Fig. 3c split, leading to well-defined male and female clusters for each brain region at P7 (Fig. 3d). With brain maturation, ♀/♂ clusters in DG_{mg}, FC_{mg} and SI_{mg} converged, while those in CB_{mg}, CN_{mg}, OB_{mg} and SN_{mg} remained distinct. To follow this sexual dimorphism along the developmental trajectory, we ordered the bootstrapped persistence images with the Palantir algorithm, which uses principles from graph theory and Markov processes to infer a pseudo-temporal trajectory (Fig. 3e). In the Palantir space, nearby points indicate similar persistence images, thereby assuming a gradual transition in their morphologies, and the continuous sequence of points define a trajectory. The developmental trajectories were similar between brain regions, with P7 and P22 clusters being the furthest from and the closest to the adult, respectively. In contrast, P15 shifted laterally from the P7–P22 trajectory and occupied the outermost position in nearly all the brain regions, indicating a unique microglial context-dependent response that coincides with neuronal circuit synapse refinement^{35–37}.

Link between morphology and response in the 5xFAD context

Synaptic loss combined with amyloid plaque deposition are common signs of Alzheimer's disease, with the neocortex and the hippocampus being the most affected brain regions³⁸. Microglial morphology alters during the progression of Alzheimer's disease³⁹ but the disease phenotype of microglia in the directly and indirectly affected brain regions, as well as the impact on the sexual dimorphism, is not entirely understood^{40,41}. To address this, we expanded our microglia with 3D-traced microglial morphologies in the 5xFAD mouse model (Fig. 4a), which recapitulates a familial form of Alzheimer's disease⁴², for all seven brain regions. We focused on animals that were 3 and 6 months old (5xFAD_{3m} and 5xFAD_{6m}, respectively; Extended Data Fig. 6a,b) because amyloid plaques occur first in the deep cortical layers at 3 months, followed by the hippocampus, coinciding with spine loss and memory deficits at around 6 months⁴². As anticipated, microglia in the 5xFAD_{3m} group exhibited a disease phenotype in which all brain regions were distinguishable from controls. The 5xFAD_{6m} group formed a 'disease-associated cluster' in the UMAP space, with the exception of CB_{mg} (Fig. 4b). SI_{mg}, FC_{mg} and DG_{mg} already occupied this disease-associated cluster in 5xFAD_{3m}. To obtain insights on which part of the microglia branching tree adapts during disease progression, we identified the representative bootstrap persistence image closest to the average for both control and 5xFAD_{6m} groups, and then subtracted them. Overall, the subtraction plots and the corresponding

representative morphology indicated increased primary branches and loss of high-level branches in 5xFAD_{6m} compared to controls (Extended Data Fig. 6c). This effect was less pronounced in the FC_{mg} and CB_{mg} cluster, suggesting a brain-region-selective microglia reactivity that might adapt in a targeted way.

Next, we included the sex of the microglia in our MorphOMiCs analysis. Microglia demonstrated higher morphological heterogeneity in 5xFAD_{6m} mice, with males partially overlapping and females spreading into clusters distinct from controls (Fig. 4c). When we applied Palantir to identify sex-dependent disease trajectories, we observed sexual dimorphism (Fig. 4d and Extended Data Fig. 7a), especially in one of the first affected brain regions, SI. ♀SI_{mg} seem to precede ♂SI_{mg}; ♀SI_{mg} clusters already overlapped in 5xFAD_{3m} mice with the trajectory that males reach only at 6 months (Fig. 4d). Such a difference was less obvious for FC_{mg} and DG_{mg}, which is likely influenced by the limited number of selected time points during the pathology. Despite this, ♀DG_{mg} and ♀FC_{mg} display a phenotypic spectrum along the disease trajectory. To link microglial phenotype to their reactivity, we performed immunostaining for the endosomal/lysosomal marker CD68 (ref. ⁴³). We then computed the fold change compared to the control CD68 volume within Iba1⁺ cells and overlaid the CD68 fold change on the Palantir trajectory (Fig. 4d). In ♀SI_{mg}, CD68 increased already at 3 months, while this only occurred in ♂SI_{mg} at 6 months, confirming that the shift along the morphological spectrum happens earlier in females. For the other brain regions, this effect was less obvious. We also applied Palantir trajectories to the other brain regions, because plaque deposition has been reported in the olfactory bulb and brainstem²³. We found a strong sexual dimorphism in microglial morphology in these brain regions, with less-obvious trajectory changes (Extended Data Fig. 7b). CB_{mg} was the only exception, remaining mainly unaffected in 5xFAD mice, which is consistent with previous literature⁴². Overall, the 5xFAD data indicate that the link between microglial disease phenotype and reactivity state depends on the brain region.

Early shift of microglial morphology in female CK-p25 mice

An alternative model with faster onset and disease progression is the CK-p25 model for sporadic Alzheimer-like degeneration⁴⁴. Upon doxycycline withdrawal, p25 expression is induced in CamKII⁺ forebrain neurons resulting in neurotoxic activity of the cyclin-dependent kinase Cdk6 (ref. ⁴⁵). Within 2 weeks, CK-p25 mice develop progressive neuronal and synaptic loss, forebrain atrophy, aberrant amyloid-precursor protein processing, hyper-phosphorylation of tau and, at later stages, neurofibrillary tangle-like pathology⁴⁴ (Fig. 5a). We reconstructed microglial morphologies from CK-p25 mice at 1, 2 and 6 weeks (CK-p25_{1w}, CK-p25_{2w} and CK-p25_{6w}, respectively; Extended Data Fig. 8a,b), included them in our library, and applied MorphOMiCs. Similarly to 5xFAD, all seven brain regions started to segregate from the control at 1 week and occupied a disease-associated cluster in CK-p25_{6w}, with CB_{mg} and CN_{mg} staying distinct (Fig. 5b). FC_{mg} reached this cluster already at 2 weeks, while OB_{mg}, DG_{mg}, SI_{mg} and SN_{mg} only at 6 weeks. When we obtained the subtraction plots between control and CK-p25_{6w}, we found that microglia in CK-p25_{6w} have lost their high-level branches and their primary branches were overrepresented compared to control suggesting a reactive phenotype (Extended Data Fig. 8c). In contrast, CB_{mg} only showed a mild response likely due to an indirect effect as CaMKII is not expressed in the cerebellum. CN_{mg} morphology was mostly unaffected.

Fig. 4 | Microglia phenotypic spectrum in 5xFAD transgenic model of neurodegeneration is sexually dimorphic. **a**, Sagittal view of analyzed brain regions with color coding. Timeline of degeneration events in the 5xFAD transgenic mouse model. **b, c**, UMAP plots of MorphOMiCs-analyzed microglia across seven brain regions (color coded) for control, 5xFAD_{3m} and 5xFAD_{6m} with both sexes (**b**) or for each sex separately (**c**). Each degeneration time point is highlighted in a separate UMAP. Each dot represents a bootstrapped persistence

image. $n_{\text{samples}} = 500$ per condition ('Average and bootstrapped persistence images'). **d**, Representative confocal images of immunostained microglia (Iba1; green) and lysosome (CD68; magenta), followed by Palantir reconstruction of microglial trajectory (top) with corresponding color-coded average CD68 fold change (bottom) across three animals from females and males for 5xFAD_{3m} and 5xFAD_{6m} in SI, FC and DG. Scale bar, 10 μm . Fold change < 0 in blue and > 0 in red. A β 42, amyloid beta.

Next, we applied MorphOMICs to the CK-p25 dataset separated by sex. We found that, in females, SN_{mg}, FC_{mg}, OB_{mg}, DG_{mg} and S1_{mg} reached the disease cluster at 6 weeks, while in males, DG_{mg} and S1_{mg} stayed distinct (Fig. 5c). Similarly, Palantir displayed a trajectory arm, on which microglial morphology from later disease stages accumulated (Extended Data Fig. 9a). Neither CN_{mg} nor CB_{mg} reached this disease-associated arm as expected, due to the low expression of CaMKII in these brain regions⁴⁶. Comparison of the sex-specific Palantir projections also showed that ♀FC_{mg} preceded ♂FC_{mg} in CK-p25_{2w} (Fig. 5d). We replicated the same dynamics with Monocle, an alternative algorithm which uses reversed graph embedding to infer a pseudo-time trajectory (Extended Data Fig. 9b)⁴⁷.

When we overlaid the CD68 fold change compared to control adults over the Palantir FC_{mg} trajectory, we found that the CD68 fold change gradually increased (Fig. 5d), suggesting a CD68 dynamic that is different from morphological adaptations. Indeed, morphological changes did not correspond to CD68 in ♀DG_{mg} and ♀S1_{mg} at 6 weeks: the morphology reached the disease-associated arm but without increased CD68 fold change. Instead, ♂DG_{mg} and ♀DG_{mg} showed their highest CD68 fold change at 2 weeks and occupied a similar cluster in the Palantir space (Fig. 5d). Together, this suggests that the microglial response might be associated with the transient effect of p25 expression, which has been shown to enhance long-term potentiation and improve hippocampus-dependent memory, before inducing neurodegeneration, gliosis and severe cognitive decline at 6 weeks⁴⁸. For those brain regions that were less affected, dimorphic microglial phenotype was less pronounced (Extended Data Fig. 9c). In both sexes, SN_{mg} and OB_{mg} in CK-p25_{6w} reached the disease-associated arm, whereas in CB_{mg} and CN_{mg}, neither sex nor disease progression influenced morphology (Extended Data Fig. 9d). Overall, the CK-p25 model exhibited strong dimorphic phenotype spectrum in favor of females, which precede their male counterparts in a brain-region-specific manner.

Morphological information extraction with MorphOMICs. So far, we established both an adult sexual dimorphic microglia phenotype and a morphological spectrum during development and degeneration for seven brain regions. To further exemplify the superior performance of MorphOMICs over morphological feature selection, we applied common classifiers to the CK-p25 FC_{mg} dataset. Neither performing pairwise statistical comparisons of time points with common classifiers (Extended Data Fig. 10a and Supplementary Table 2) nor applying bootstrapping approaches to an extended set of non-interdependent morphometric quantities (Fig. 6a and Supplementary Table 3) replicated the sexually dimorphic control-to-disease spectrum from Fig. 5d. Similarly, we observed the same information loss for FC_{mg} in the 5xFAD model and during development (Extended Data Fig. 10b,c), although microglia from adult brain regions segregate (Extended Data Fig. 10d), suggesting that MorphOMICs preserves certain intrinsic properties of the reconstructed tree after dimensionality reduction.

To identify which properties are potentially relevant, we looked at the most variable pixels across CK-p25 FC_{mg} and the control bootstrapped persistence images (Fig. 6b). We found the highest variability along the diagonal and close to origin of the persistence diagram corresponding to short branches and branches close to the soma (Fig. 1b). We therefore decided to zoom in on the short and the long persistence bars, filtered them out separately, and repeated our MorphOMICs

analysis (Fig. 6c–f). Using this method, we saw those bars corresponding to primary processes, sufficed to capture the sexually dimorphic phenotypes along the disease trajectory that we have previous seen (Fig. 6e). Interestingly, when we focused only on the short bars, reflecting short terminal processes, we found that males aggregated across all time points in a corner, whereas the females gradually adapted (Fig. 6f). These results suggest that persistence barcodes highlight different phenomena, and therefore both short and long bars are essential for the understanding of morphology.

Atlas of context-dependent and cue-dependent microglial phenotypes

Until now, we have treated microglial morphology separately for development and disease. As both conditions induce a shift along the morphological spectrum, we were interested in how these conditions integrate along the pseudo-temporal trajectory to form a microglia reactivity spectrum. To achieve this, we performed MorphOMICs for each brain region and sex separately, including all developmental and disease time points and extracted the trajectory with Palantir (Fig. 7a,b). We first focused on the female reactivity spectra for FC_{mg} and DG_{mg} (Fig. 7a). In ♀FC_{mg}, the P7, P15, P22, 5xFAD_{3m} and 5xFAD_{6m} groups aligned together reaching out toward the CK-p25_{2w} and CK-p25_{6w} groups, which extends away from all the other conditions, forming a disease-associated arm. Interestingly, ♀DG_{mg} mimicked a similar spectrum but with both 5xFAD and early CK-p25 forming a cluster distant from the P15 and the control, and the P7 group reaching out toward CK-p25_{6w}. In both regions, microglia in 5xFAD_{6m} never reach the disease-associated arm suggesting a milder environmental condition compared to the late stages of CK-p25 neurodegeneration.

In males, disease phenotypes evolved more slowly than in females, with only ♂FC_{mg} reaching the disease-associated arm at CK-p25_{6w} (Fig. 7b). Like in females, we observed both 5xFAD groups close to the control together with P15, followed by intermingled P7, P22 and CK-p25_{1w}. In ♂DG, microglial morphologies from P7 and CK-p25_{1w} clustered together, segregating from the rest of the conditions. Overall, ♂DG_{mg} displayed a similar phenotypic spectrum compared to ♂FC_{mg} for both 5xFAD groups, shifting toward the CK-p25_{2w}–CK-p25_{6w} cluster. In the CB, both ♀ and ♂ CB_{mg} did not show any clear trajectory progression. Whereas the disease clusters mostly intermingled with the control, suggesting only a minor response to the disease environment, the developmental time points were distinct to the control (Fig. 7). Overall, our data show that microglia display a spectrum of phenotypes, with developmental time points occupying distinct parts of the trajectory in a brain-region-dependent manner.

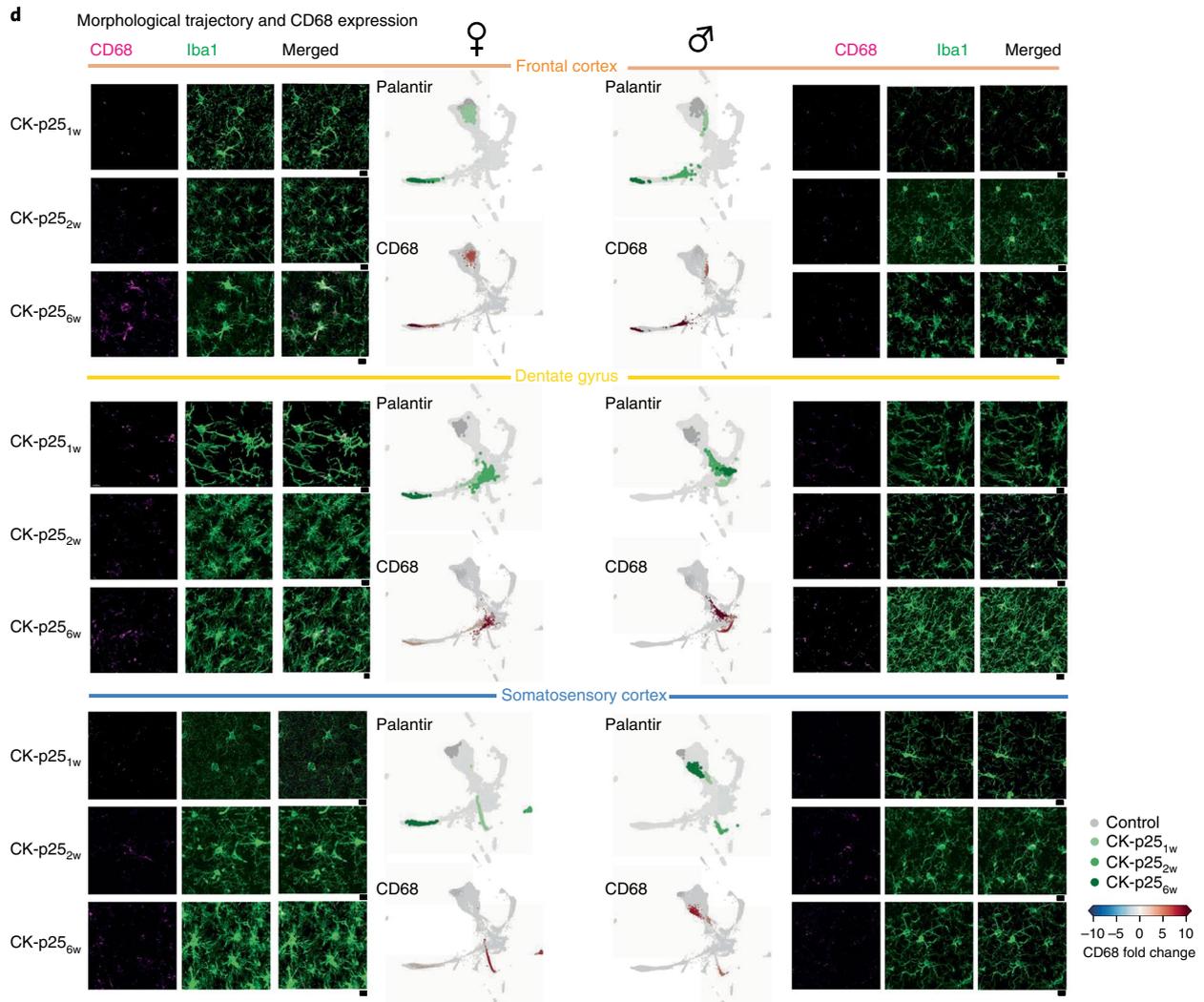
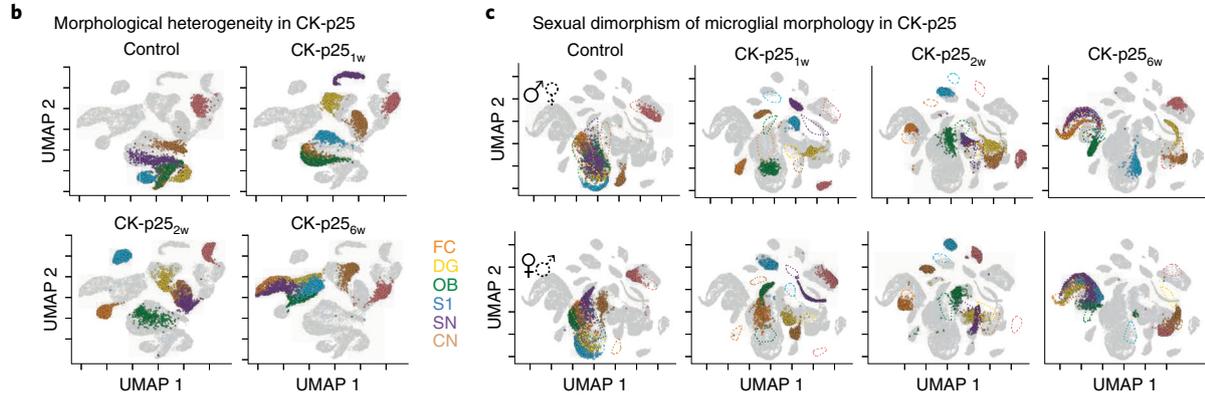
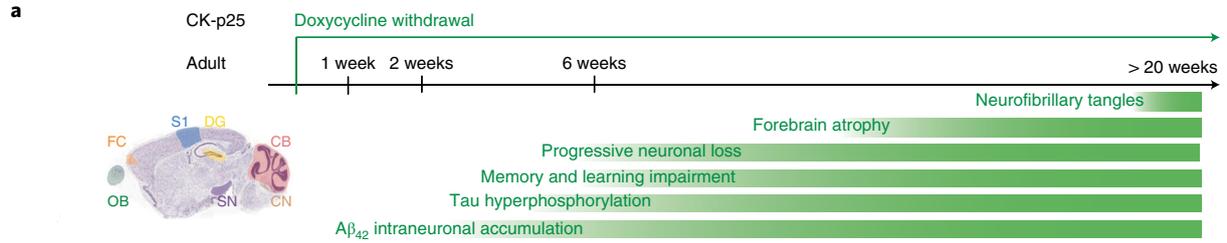
Morpho-functional relationship after repeated ketamine

We built a comprehensive library of 3D-traced microglia that, in combination with MorphOMICs, resolved a reactivity spectrum that can serve as a reference atlas for future addition of microglial morphologies (Extended Data Figs. 10e and 8a). To demonstrate the utility of such an atlas, we focused on S1 and used linear regression to estimate the location of the Palantir coordinates within a larger atlas with 2,000 bootstrapped persistence images per condition (Fig. 8a). As a first proof of concept, we generated new sets of bootstrapped images in all conditions and successfully mapped them to their corresponding clusters (Fig. 8b).

Fig. 5 | The microglia phenotype of females in CK-p25 model of neurodegeneration exhibit an earlier morphological shift than in males.

a, Sagittal view of analyzed brain regions with color coding. Timeline of degeneration events upon doxycycline withdrawal in the CK-p25 transgenic mouse model. **b,c**, UMAP plots displaying microglial morphological heterogeneity in adult control mice and CK-p25 mice at 1, 2 and 6 weeks after doxycycline withdrawal across all the analyzed brain regions for both sexes (**b**) or for each sex separately (**c**). Each dot represents a bootstrapped

persistence image, and each UMAP highlights a distinct degeneration time point. $n_{\text{samples}} = 500$ per condition ('Average and bootstrapped persistence images'). **d**, Representative confocal images of immunostained microglia (Iba1; green) and lysosomes (CD68; magenta) in CK-p25 mice at 1, 2 and 6 weeks after doxycycline withdrawal in FC, DG and S1. Scale bar, 10 μm . Palantir reconstruction of microglial trajectory (top) with corresponding color-coded average CD68 fold change (bottom) across three animals. Females, left. Males, right. Fold change < 0 in blue and > 0 in red.



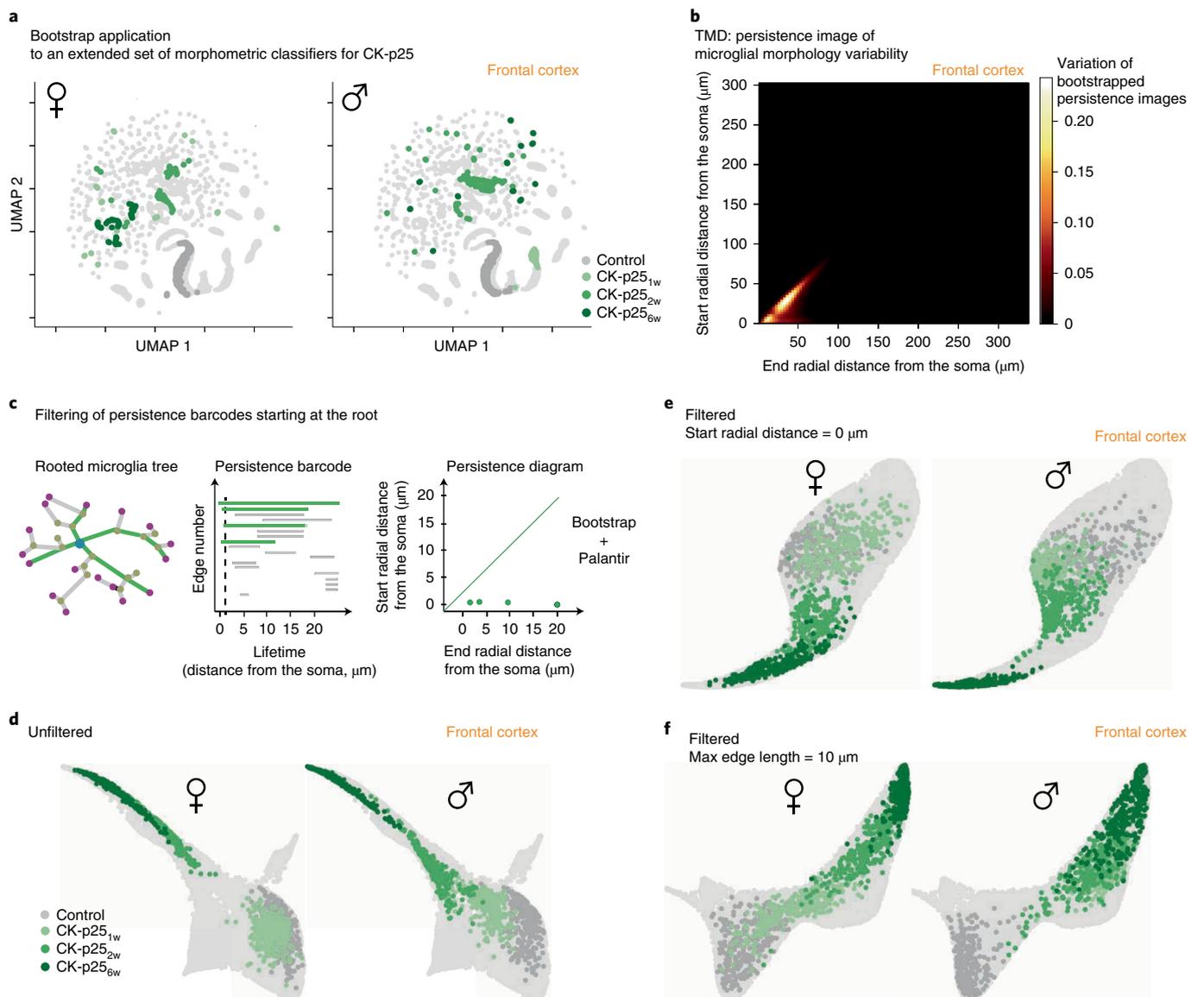


Fig. 6 | MorphOMICs applied to primary processes reiterates sexual dimorphism in CK-p25 mice. a, Bootstrapping and UMAP representations of an extended set of morphological classifiers (Supplementary Table 4) for control, CK-p25_{1w}, CK-p25_{2w} and CK-p25_{6w} female and male mice across all brain regions (without cochlear nucleus and cerebellum for simplicity). The frontal cortex is highlighted. Each dot represents an averaged extended set of morphometric classifiers across 30 microglia that form the bootstrap population. **b**, Heat map of the bootstrapped persistence images pixel-wise standard variation across control and CK-p25 conditions of the frontal cortex. Black denotes no variation;

white denotes high variation. **c**, Schematic for filtering persistence barcodes with MorphOMICs. Starting from microglial rooted tree, only bars are selected that are born at 0 μm independent of their length (representing likely primary branches, green), and are converted into a persistence diagram. **d-f**, Palantir trajectory of all brain regions (without cochlear nucleus and cerebellum for simplicity) from control and CK-p25 condition with highlighted FC microglia trajectory for females and males with unfiltered bars (**d**) or filtered bars (**e**, start radial distance from the soma, 0 μm ; **f**, maximum bar length, 10 μm). $n_{\text{samples}} = 300$ per condition ('Average and bootstrapped persistence images').

Next, we have recently shown a microglia-mediated extracellular matrix remodeling upon repeated exposure with the anesthetic ketamine¹⁰. Such treatment results in a dose-dependent microglia-mediated loss of the perineuronal net in the S1 and induces changes in plasticity¹⁰. However, we were not able to resolve morphological changes by eye (Fig. 8d). Thus, we used 3D-traced microglia in the S1 of adult C57BL/6J mice after 1 \times , 2 \times and 3 \times KXA treatment as well as after 3 d, 1 week and 2 weeks of recovery following the 3 \times KXA exposure, applied MorphOMICs and mapped their positions on the S1 reference atlas (Fig. 8b). Consistent with our previously reported dosage-dependent effect, 1 \times KXA did not lead to morphological adaptation, while with each additional dosage the microglial morphology gradually connected to the reactivity spectrum. In parallel,

CD68 expression further upregulated with each additional dosage (Fig. 8c,d). This shows that MorphOMICs provides the fundamentals for a morphology–function relationship, which could not be uncovered otherwise. Remarkably, MorphOMICs provides also a readout of microglial morphology adaptations following withdrawal after 3 \times KXA, which we have shown to reinstate the perineuronal net¹⁰. First, the morphology regresses toward the control phenotype after a 3-d recovery (Fig. 8b). Then, the microglial morphology separates on a trajectory, which diverges from the control and the KXA-treated ones suggesting a recovery-associated microglial phenotype. To gain insights on the morphological changes, we subtracted the control bootstrapped persistence image with the 2-week recovery (Fig. 8e). The recovery-associated microglia displayed more short processes

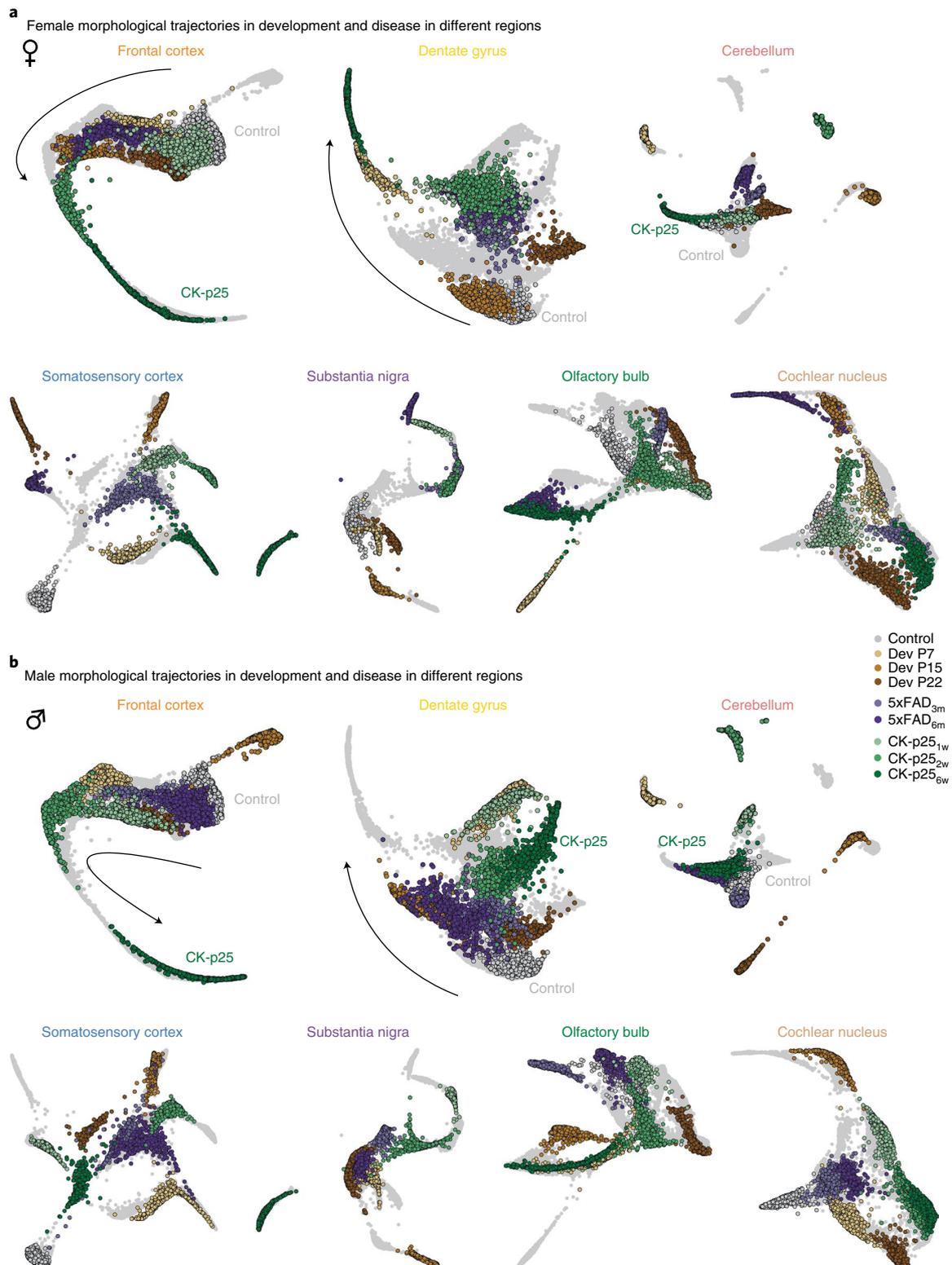


Fig. 7 | Development and disease phenotypes integrate into a reactivity spectrum. a,b, Palantir reconstructions calculated independently for each brain region for control, P7, P15, P22, CK-p25_{1w}, CK-p25_{2w}, CK-p25_{6w}, 5xFAD_{3m} and

5xFAD_{6m} male and female mice. Microglial trajectory is highlighted for females (**a**) and males (**b**). Black arrow, control-to-disease spectrum. $n_{\text{samples}} = 200$ per condition ('Average and bootstrapped persistence images').

closer to but not emanating from the soma, pointing toward a hyper-ramification. Overall, the combination of our reference atlas and MorphOMICs provides first insights into microglial morphology and their functional response.

Discussion

In this study, we analyzed heterogeneity and sexual dimorphism of microglia morphology across seven brain regions from 41,872 cells through development, disease and under repeated ketamine exposure

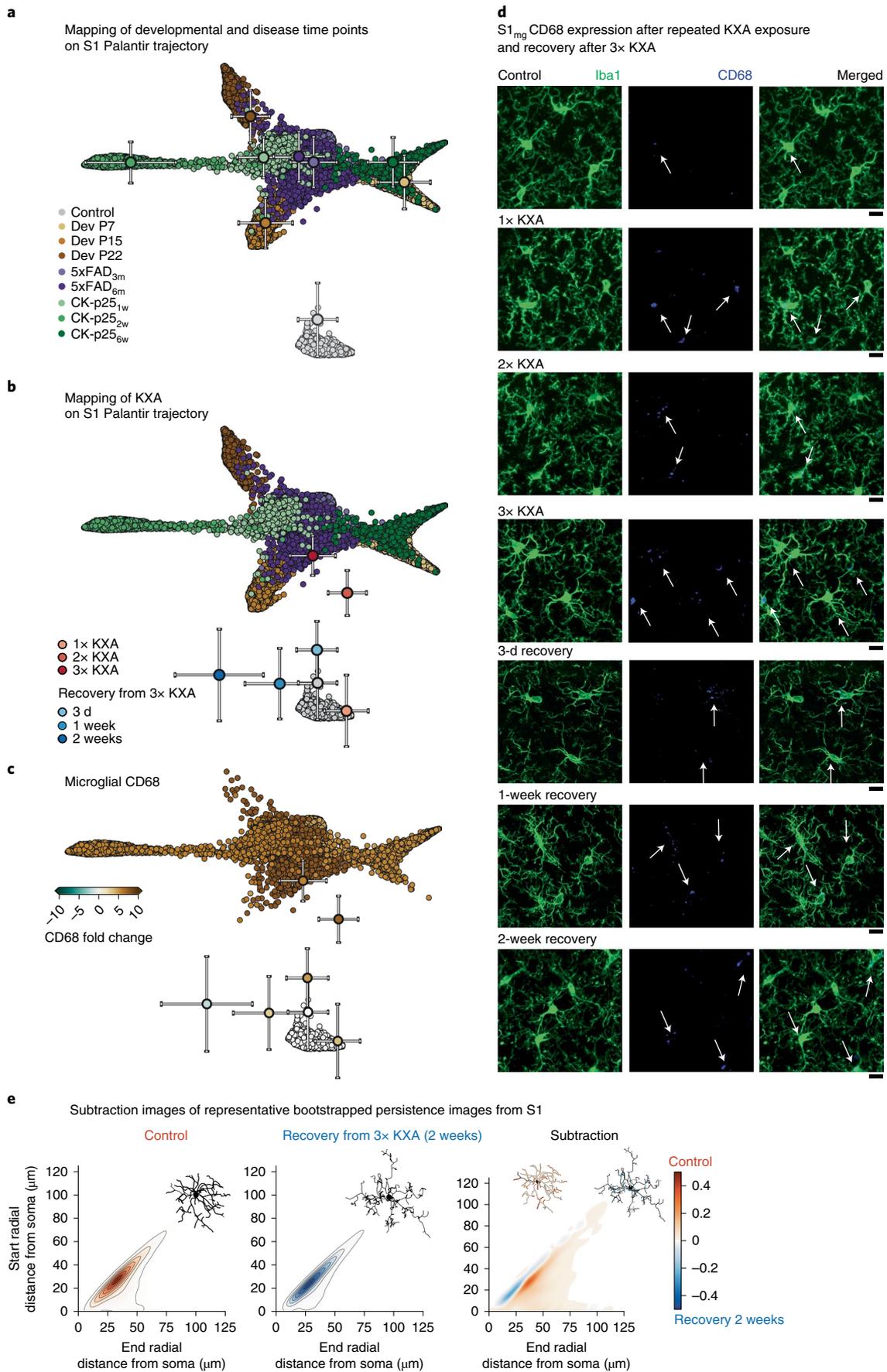


Fig. 8 | MorphOMICs applied to KXA-treated microglia. **a**, Mapping of S1 microglial morphology on Palantir trajectory. Centroids indicating the mean position of mapped points in a given condition with the corresponding standard deviations. **b**, Palantir reconstruction of microglia morphological trajectory in S1 from adult control, P7, P15, P22, 5xFAD_{3m}, 5xFAD_{6m}, CK-p25_{1w}, CK-p25_{2w} and CK-p25_{6w} after 1×, 2× and 3× KXA and 3× KXA recovery after 3 d, 1 week and 2 weeks. Centroids indicate the mean position of mapped points in a given condition with the corresponding standard deviations. $n_{\text{samples}} = 300$ per condition ('Average and bootstrapped persistence images'). **c**, Corresponding color-coded average CD68

fold change across three animals. Fold change, blue < 0; brown > 0. **d**, Representative confocal images of immunostained microglia (Iba1; green) and endosomal/lysosomal CD68 (blue) from control, 1×, 2× and 3× KXA and 3× KXA recovery after 3 d, 1 week and 2 weeks from the S1. Arrows indicate CD68 inside of microglia. Scale bar, 10 μm . **e**, Representative persistence images corresponding to control and 3× KXA_{2w} centroids from **b** with color-coded process density. Top-right corner: representative traced microglia. Subtraction image with highlighted overrepresented processes on the representative microglia.

and recovery (Supplementary Tables 4 and 5). To establish a reference atlas of morphological phenotypes, we developed and applied the MorphOMICs pipeline, which extracts the information of the entire reconstructed microglial tree in a minimally biased way, combined with variability reduction and data visualization.

MorphOMICs takes advantage of applied topology and preserves the intrinsic properties of the reconstructed morphological tree avoiding feature-selection-derived biases. Contrary, classical morphometric classifiers include only user-selected features and there has been open debate about which classifier reliably describes the morphological phenotype of microglia. Recent studies have explored the options of alternative machine learning paradigms to identify phenotypic differences; however, they rely on a priori-labeled datasets and/or morphological feature selection^{3,49,50}. MorphOMICs is independent of such assumptions. Furthermore, we demonstrate that commonly used morphometrics like process length, number of branches, terminal points or branching points failed to separate cells from different conditions (Extended Data Figs. 1a and 10a). Due to interdependency of these parameters, we expanded the list to 27 diverse classifiers (Supplementary Table 3)⁵¹ and applied bootstrap and dimensionality reduction, but even these parameters were insufficient to resolve differences in microglia morphology in CK-p25 (Fig. 6a), 5xFAD (Extended Data Fig. 10b) or postnatal development (Extended Data Fig. 10c). Similarly, Sholl curves could not fully recapitulate the spatial heterogeneity, and the radius step size influences the readout (Extended Data Fig. 3b,c). Interestingly, we found that both long primary processes and short terminal processes contain information that contribute to the microglial spectrum (Fig. 6c–f) emphasizing the importance of retaining as many features as possible. Classical morphometrics and Sholl curves are suboptimal for this.

Brain-region-specific single-cell transcriptome analyses have pointed toward microglial functional heterogeneity^{52–54}, but morphological differences have so far been difficult to identify. MorphOMICs revealed that microglia in an adult brain exhibit regional heterogeneity (Fig. 1f) that exists already in early postnatal development (Fig. 3c) and diminishes during degeneration (Figs. 4b and 5b). Although microglia display a phenotypic spectrum (Fig. 7), they respond to diseases in a brain-region-dependent manner. Moreover, we confirmed that a sex-specific phenotype exists, which has long been debated²⁹. This effect is rather mild during adulthood (Fig. 2b) but prominent during development (Fig. 3d) and degeneration (Figs. 4c and 5c). Both degeneration models showed a sexually dimorphic microglial response, which was pronounced in the immediately affected brain regions. Females showed an earlier shift along the morphological spectrum compared to males. This supports studies that have suggested a sex-dependent difference in Alzheimer's disease progression^{40,41,55} and points to females having a higher risk of developing dementia^{56,57}.

Estrogens have been shown to be involved in the masculinization of the brain^{58,59}, and microglia are suspected of playing a role in this process⁵⁸. Surprisingly, in the ovariectomized females, microglia are distinct from their non-ovariectomized counterparts and the brain regions intermingled differently (Fig. 2c). Whereas ♀FC_{mg} and ♀OB_{mg} occupied a similar cluster in control adults, ♀_{ov}FC_{mg} were distinct from ♀_{ov}OB_{mg} and highly intermingled with ♀_{ov}SN_{mg} (Fig. 2c), suggesting

that the impact of estrogens on microglial morphology is complex. Overall, MorphOMICs links the previously reported sexually dimorphic microglial transcriptome in the healthy brain^{60–63} and in degeneration models^{64–68} with a distinct morphological phenotype.

We showed that MorphOMICs detects microglial morphological changes at high resolution in several physiological conditions deviating from adult controls. For example, microglia shifted at P15 from the P7/P22 trajectory across all brain regions (Fig. 3e). This is the time of circuit refinement, where microglia have frequently been shown to participate in synaptic pruning^{36,37}. Another synapse-associated pattern occurred in the DC_{mg} of CK-p25_{2w} (Fig. 5d). Unexpectedly, we found here the highest CD68 fold change and not within the CK-p25_{6w}, where we have observed the most distinct morphological shift from the control. This discrepancy might be associated with previously observed transient p25 expression⁴⁸. In general, we could not associate CD68 upregulation with a distinct microglia response phenotype.

MorphOMICs provides the fundamentals to track subtle morphological changes that can be important indicators of local environmental changes and interference with the neuronal network. Whereas we have not found any obvious changes in the microglia morphology upon repeated ketamine anesthesia or the recovery (Fig. 8d), MorphOMICs overcomes the ambiguity and strongly predicts a microglia response based on our reference atlas (Fig. 8b) that can be investigated in a targeted manner. MorphOMICs provides an advanced strategy for systematically comparing microglial populations across different brain regions and conditions: this could be expanded infinitely. Future studies will focus on identifying informative regions of a persistence barcode, which provides a perspective for morphological analysis of lower-resolution images, such as in vivo microglial imaging for potential noninvasive diagnostic applications. Stable ranks would provide a mathematically robust approach to address this question, as we have shown that standard stable ranks of the TMD captured the microglial phenotypes (Extended Data Figs. 2h and 3a) as well as the persistence images of the microglial TMD (Fig. 1f). A critical point to consider is the number of cells that are needed for MorphOMICs. While we identified a suitable bootstrap size in Extended Data Fig. 2d, the condition-specific variability in microglial morphology needs to be systematically assessed to determine the minimum cell number before MorphOMICs can be reliably applied.

MorphOMICs overcomes the dichotomized view of microglial morphology to either ramified, relating to a surveilling function, or amoeboid, for participation in phagocytosis.

We anticipate that future studies will build on MorphOMICs and our atlas and will incorporate the epigenetic, transcriptional and/or proteomic landscapes along the microglial phenotypic spectrum. This will substantially advance our knowledge of the interplay between microglia and the nervous system.

Online content

Any methods, additional references, Nature Research reporting summaries, source data, extended data, supplementary information, acknowledgements, peer review information; details of author contributions and competing interests; and statements of data and code availability are available at <https://doi.org/10.1038/s41593-022-01167-6>.

References

- Gouwens, N. W. et al. Classification of electrophysiological and morphological neuron types in the mouse visual cortex. *Nat. Neurosci.* **22**, 1182–1195 (2019).
- Morrison, H. W. & Filosa, J. A. A quantitative spatiotemporal analysis of microglia morphology during ischemic stroke and reperfusion. *J. Neuroinflammation* **10**, 4 (2013).
- Heindl, S. et al. Automated morphological analysis of microglia after stroke. *Front. Cell. Neurosci.* **12**, 106 (2018).
- Kongsui, R., Beynon, S. B., Johnson, S. J. & Walker, F. R. Quantitative assessment of microglial morphology and density reveals remarkable consistency in the distribution and morphology of cells within the healthy prefrontal cortex of the rat. *J. Neuroinflammation* **11**, 182 (2014).
- Tan, Y. L., Yuan, Y. & Tian, L. Microglial regional heterogeneity and its role in the brain. *Mol. Psychiatry* **25**, 351–367 (2019).
- Stratoulas, V., Venero, J. L., Tremblay, M. & Joseph, B. Microglial subtypes: diversity within the microglial community. *EMBO J.* **38**, e101997 (2019).
- Bachstetter, A. D. et al. Disease-related microglia heterogeneity in the hippocampus of Alzheimer's disease, dementia with Lewy bodies, and hippocampal sclerosis of aging. *Acta Neuropathol. Commun.* **3**, 32 (2015).
- Paolicelli, R. C. et al. Synaptic pruning by microglia is necessary for normal brain development. *Science* **333**, 1456–1458 (2011).
- Pont-Lezica, L., Béchade, C., Belarif-Cantaut, Y., Pascual, O. & Bessis, A. Physiological roles of microglia during development. *J. Neurochem.* **119**, 901–908 (2011).
- Venturino, A. et al. Microglia enable mature perineuronal nets disassembly upon anesthetic ketamine exposure or 60-Hz light entrainment in the healthy brain. *Cell Rep.* **36**, 109313 (2021).
- Carlsson, G. Topology and data. *Bull. Am. Math. Soc.* **46**, 255–308 (2009).
- Davalos, D. et al. Stable in vivo imaging of densely populated glia, axons and blood vessels in the mouse spinal cord using two-photon microscopy. *J. Neurosci. Methods* **169**, 1–7 (2008).
- Nimmerjahn, A., Kirchhoff, F. & Helmchen, F. Resting microglial cells are highly dynamic surveillants of brain parenchyma in vivo. *Science* **308**, 1314–1318 (2005).
- Kanari, L. et al. A topological representation of branching neuronal morphologies. *Neuroinformatics* **16**, 3–13 (2017).
- Li, Y., Wang, D., Ascoli, G. A., Mitra, P. & Wang, Y. Metrics for comparing neuronal tree shapes based on persistent homology. *PLoS ONE* **12**, e0182184 (2017).
- Ito, D. et al. Microglia-specific localisation of a novel calcium binding protein, Iba1. *Brain Res. Mol. Brain. Res.* **57**, 1–9 (1998).
- Jacobs, H. I. L. et al. The cerebellum in Alzheimer's disease: evaluating its role in cognitive decline. *Brain* **141**, 37–47 (2018).
- Sinha, U. K., Hollen, K. M., Rodriguez, R. & Miller, C. A. Auditory system degeneration in Alzheimer's disease. *Neurology* **43**, 779–779 (1993).
- Brar, S., Henderson, D., Schenck, J. & Zimmerman, E. A. Iron accumulation in the substantia nigra of patients with Alzheimer disease and parkinsonism. *Arch. Neurol.* **66**, 371–374 (2009).
- Wiesman, A. I. et al. Somatosensory dysfunction is masked by variable cognitive deficits across patients on the Alzheimer's disease spectrum. *EBioMedicine* **73**, 103638 (2021).
- Thompson, P. M. et al. Mapping hippocampal and ventricular change in Alzheimer disease. *Neuroimage* **22**, 1754–1766 (2004).
- Leuba, G. et al. Differential changes in synaptic proteins in the Alzheimer frontal cortex with marked increase in PSD-95 postsynaptic protein. *J. Alzheimers Dis.* **15**, 139–151 (2008).
- Struble, R. G. & Clark, H. B. Olfactory bulb lesions in Alzheimer's disease. *Neurobiol. Aging* **13**, 469–473 (1992).
- Kozłowski, C. & Weimer, R. M. An automated method to quantify microglia morphology and application to monitor activation state longitudinally in vivo. *PLoS ONE* **7**, e31814 (2012).
- Zusso, M. et al. Regulation of postnatal forebrain amoeboid microglial cell proliferation and development by the transcription factor runx1. *J. Neurosci.* **32**, 11285–11298 (2012).
- Adams, H. et al. Persistence images: a stable vector representation of persistent homology. *J. Mach. Learn. Res.* **18**, 1–35 (2017).
- Van Der Maaten, L. & Hinton, G. Visualizing data using t-SNE. *J. Mach. Learn. Res.* **9**, 2579–2605 (2008).
- Sholl, D. A. Dendritic organization in the neurons of the visual and motor cortices of the cat. *J. Anat.* **87**, 387–406 (1953).
- Nelson, L. H., Warden, S. & Lenz, K. M. Sex differences in microglial phagocytosis in the neonatal hippocampus. *Brain Behav. Immun.* **64**, 11–22 (2017).
- Han, J., Fan, Y., Zhou, K., Blomgren, K. & Harris, R. A. Uncovering sex differences of rodent microglia. *J. Neuroinflammation* **18**, 74 (2021).
- Caligioni, C. S. Assessing reproductive status/stages in mice. *Curr. Protoc. Neurosci.* **48**, A–41 (2009).
- Ginhoux, F. et al. Fate mapping analysis reveals that adult microglia derive from primitive macrophages. *Science* **330**, 841–845 (2010).
- Ben-Ari, Y. Excitatory actions of GABA during development: the nature of the nurture. *Nat. Rev. Neurosci.* **3**, 728–739 (2002).
- Perez-Pouchoulen, M., VanRyzin, J. W. & McCarthy, M. M. Morphological and phagocytic profile of microglia in the developing rat cerebellum. *eNeuro* **2**, 36–51 (2015).
- Yang, J. M., Zhang, J., Yu, Y. Q., Duan, S. & Li, X. M. Postnatal development of two microcircuits involving fast-spiking interneurons in the mouse prefrontal cortex. *Cereb. Cortex* **24**, 98–109 (2014).
- Wong, T. et al. Postnatal development of intrinsic GABAergic rhythms in mouse hippocampus. *Neuroscience* **134**, 107–120 (2005).
- Kroon, T., van Hugte, E., van Linge, L., Mansvelter, H. D. & Meredith, R. M. Early postnatal development of pyramidal neurons across layers of the mouse medial prefrontal cortex. *Sci. Rep.* **9**, 5037 (2019).
- Serrano-Pozo, A., Frosch, M. P., Masliah, E. & Hyman, B. T. Neuropathological alterations in Alzheimer disease. *Cold Spring Harb. Perspect. Med.* **1**, a006189 (2011).
- Hemonnot, A. L., Hua, J., Ulmann, L. & Hirbec, H. Microglia in Alzheimer disease: well-known targets and new opportunities. *Front. Aging Neurosci.* **11**, 233 (2019).
- Gamache, J., Yun, Y. & Chiba-Falek, O. Sex-dependent effect of APOE on Alzheimer's disease and other age-related neurodegenerative disorders. *Dis. Model. Mech.* **13**, dmm045211 (2020).
- Manji, Z. et al. 5xFAD mice display sex-dependent inflammatory gene induction during the prodromal stage of Alzheimer's disease. *J. Alzheimers Dis.* **70**, 1259–1274 (2019).
- Oakley, H. et al. Intraneuronal β -amyloid aggregates, neurodegeneration, and neuron loss in transgenic mice with five familial Alzheimer's disease mutations: potential factors in amyloid plaque formation. *J. Neurosci.* **26**, 10129–10140 (2006).
- Chistiakov, D. A., Killingsworth, M. C., Myasoedova, V. A., Orekhov, A. N. & Bobryshev, Y. V. CD68/macrosialin: not just a histochemical marker. *Lab. Invest.* **97**, 4–13 (2017).
- Cruz, J. C. et al. p25/cyclin-dependent kinase 5 induces production and intraneuronal accumulation of amyloid- β in vivo. *J. Neurosci.* **26**, 10536–10541 (2006).

45. Camins, A., Verdaguer, E., Folch, J., Canudas, A. M. & Pallàs, M. The role of CDK5/P25 formation/inhibition in neurodegeneration. *Drug News Perspect.* **19**, 453–460 (2006).
46. Wang, X., Zhang, C., Szábo, G. & Sun, Q. Q. Distribution of CaMKII α expression in the brain in vivo, studied by CaMKII α -GFP mice. *Brain Res.* **1518**, 9–25 (2013).
47. Trapnell, C. et al. The dynamics and regulators of cell fate decisions are revealed by pseudotemporal ordering of single cells. *Nat. Biotechnol.* **32**, 381–386 (2014).
48. Fischer, A., Sananbenesi, F., Pang, P. T., Lu, B. & Tsai, L. H. Opposing roles of transient and prolonged expression of p25 in synaptic plasticity and hippocampus-dependent memory. *Neuron* **48**, 825–838 (2005).
49. Salamanca, L. et al. MIC-MAC: an automated pipeline for high-throughput characterization and classification of three-dimensional microglia morphologies in mouse and human postmortem brain samples. *Glia* **67**, 1496–1509 (2019).
50. Del Mar Fernández-Arjona, M. et al. Microglia morphological categorization in a rat model of neuroinflammation by hierarchical cluster and principal-components analysis. *Front. Cell. Neurosci.* **11**, 235 (2017).
51. Bijari, K., Valera, G., López-Schier, H. & Ascoli, G. A. Quantitative neuronal morphometry by supervised and unsupervised learning. *STAR Protoc.* **2**, 100867 (2021).
52. Mildner, A. et al. Distinct and non-redundant roles of microglia and myeloid subsets in mouse models of Alzheimer's disease. *J. Neurosci.* **31**, 11159–11171 (2011).
53. Furube, E., Kawai, S., Inagaki, H., Takagi, S. & Miyata, S. Brain-region-dependent heterogeneity and dose-dependent difference in transient microglia population increase during lipopolysaccharide-induced inflammation. *Sci. Rep.* **8**, 2203 (2018).
54. Grabert, K. & McColl, B. W. Isolation and phenotyping of adult mouse microglial cells. *Methods Mol. Biol.* **1784**, 77–86 (2018).
55. Congdon, E. E. Sex differences in autophagy contribute to female vulnerability in Alzheimer's disease. *Front. Neurosci.* **12**, 372 (2018).
56. Payami, H. et al. Gender difference in apolipoprotein E—associated risk for familial Alzheimer disease: a possible clue to the higher incidence of Alzheimer disease in women. *Am. J. Hum. Genet.* **58**, 803–811 (1996).
57. Turner, R. S. Alzheimer's disease in man and transgenic mice: females at higher risk. *Am. J. Pathol.* **158**, 797–801 (2001).
58. Lenz, K. M. & McCarthy, M. M. A starring role for microglia in brain sex differences. *Neuroscientist* **21**, 306–321 (2015).
59. Nissen, J. C. Microglial function across the spectrum of age and gender. *Int. J. Mol. Sci.* **18**, 561 (2017).
60. Villa, A. et al. Sex-specific features of microglia from adult mice. *Cell Rep.* **23**, 3501–3511 (2018).
61. Thion, M. S. et al. Microbiome Influences prenatal and adult microglia in a sex-specific manner. *Cell* **172**, 500–516 (2018).
62. Schwarz, J. M., Sholar, P. W. & Bilbo, S. D. Sex differences in microglial colonization of the developing rat brain. *J. Neurochem.* **120**, 948–963 (2012).
63. Ayata, P. et al. Epigenetic regulation of brain-region-specific microglia clearance activity. *Nat. Neurosci.* **21**, 1049–1060 (2018).
64. Villa, A., Rizzi, N., Vegeto, E., Ciana, P. & Maggi, A. Estrogen accelerates the resolution of inflammation in macrophagic cells. *Sci. Rep.* **5**, 15224 (2015).
65. Vegeto, E. et al. The endogenous estrogen status regulates microglia reactivity in animal models of neuroinflammation. *Endocrinology* **147**, 2263–2272 (2006).
66. Yanguas-Casás, N. et al. Sex differences in the phagocytic and migratory activity of microglia and their impairment by palmitic acid. *Glia* **66**, 522–537 (2018).
67. Crain, J. M. & Watters, J. J. Estrogen and P2 purinergic receptor systems in microglia: therapeutic targets for neuroprotection. *Open Drug Discov. J.* **2**, 148–167 (2010).
68. Bruce-Keller, A. J. et al. Antiinflammatory effects of estrogen on microglial activation. *Endocrinology* **141**, 3646–3656 (2000).

Publisher's note Springer Nature remains neutral with regard to jurisdictional claims in published maps and institutional affiliations.

Open Access This article is licensed under a Creative Commons Attribution 4.0 International License, which permits use, sharing, adaptation, distribution and reproduction in any medium or format, as long as you give appropriate credit to the original author(s) and the source, provide a link to the Creative Commons license, and indicate if changes were made. The images or other third party material in this article are included in the article's Creative Commons license, unless indicated otherwise in a credit line to the material. If material is not included in the article's Creative Commons license and your intended use is not permitted by statutory regulation or exceeds the permitted use, you will need to obtain permission directly from the copyright holder. To view a copy of this license, visit <http://creativecommons.org/licenses/by/4.0/>.

© The Author(s) 2022

Methods

Animals

C57BL/6J (no. 000664) and B6.129P-Cx3cr1^{tm1Litt}/J (no. 005582, named here Cx3cr1^{GFP/+}, only heterozygous were used) mice were purchased from The Jackson Laboratory. All animals were housed in the ISTA Preclinical Facility, under a 12-h light–dark cycle, with food and water provided ad libitum. Animals from both sexes were used. The number of animals used for each condition is detailed in Supplementary Table 5. All animal procedures were approved by the Bundesministerium für Wissenschaft, Forschung und Wirtschaft (bmfwf) Tierversuchsgesetz 2012, BGBl (I Nr. 114/2012, idF BGBl. I Nr. 31/2018 under the nos. 66.018/0005-WF/V/3b/2016, 66.018/0010-WF/V/3b/2017, 66.018/0025-WF/V/3b/2017, 66.018/0001_V/3b/2019 and 2020-0.272.234).

5xFAD and CK-p25 mice were obtained from the Tsai laboratory at Massachusetts Institute of Technology (MIT). All animal work was approved by the Committee for Animal Care of the Division of Comparative Medicine at MIT. 5xFAD mice (B6SJL-Tg(APPsw^{FILon},PSEN1^{M146L}L286V)6799Vas/Mmjax, stock no. 34840-JAX) were obtained from The Jackson Laboratory. CK-p25 mice⁶⁹ were generated by breeding CaMKII α promoter-tTA mice (CK controls) (B6;CBA-Tg(Camk2a-tTA)1Mmay/J, Jackson Laboratory, stock no. 003010) with tetO-CDK5R1/GFP mice (C57BL/6-Tg(tetO-CDK5R1/GFP)337Lht/J, Jackson Laboratory, stock no. 005706). CK-p25 mice were conceived and raised in the presence of doxycycline-containing food to repress p25 transgene expression. To induce p25 transgene expression, mice were fed a normal rodent diet. p25 transgene expression was induced in adult mice at the age of 3 months. For MorphOMICs, we compared CK-p25 brains upon drug withdrawal with our reference C57BL/6J adult microglia population. Notably, doxycycline withdrawal might affect the gut microbiome⁷⁰, which can influence the microglial population in the brain and could cause some variability.

Mice were housed in groups of three to five on a standard 12-h light/12-h dark cycle, and all experiments were performed during the light cycle. Food and water were provided ad libitum.

Brain samples and analyzed brain regions

We analyzed brains of both sexes from C57BL/6J adult mice (8–12 weeks) exposed to 1 \times , 2 \times or 3 \times KXA (100 mg per kg body weight ketamine, MSD Animal Health, A137A01; 10 mg per kg body weight xylazine, AniMedica, 7630517; 3 mg per kg body weight acepromazine, VANA, 18F211) and recovered 3 d, 1 week and 2 weeks after 3 \times KXA⁷¹; Cx3cr1^{GFP/+} mice at P7, P15 and P21; 5xFAD mice after 3 and 6 months; and CK-p25 mice 1, 2 and 6 weeks after doxycycline withdrawal. We focused on the following brain regions: the glomerular layer of the olfactory bulb (OB), cortical layer III–V of the frontal cortex (FC) and the primary somatosensory cortex (S1), the dentate gyrus of the hippocampus (DG), the substantia nigra (SN), the cochlear nucleus (CN) and the third lobe of the cerebellum (CB). The sagittal view of the brain sections analyzed (Figs. 1–5 and Extended Data Fig. 5a) was taken from the Allen Developing Mouse Brain Atlas–Sagittal and modified to show brain regions of interest⁷².

Ovariectomy

Adolescent C57BL/6J females at P20 were anesthetized with 5% isoflurane in 0.5 l min⁻¹ O₂ during the anesthesia induction and 2% isoflurane in 0.5 l min⁻¹ O₂ during the maintenance phase. Using an electric razor, the fur was shaved to expose the skin over the lumbar spine and the region was sterilized with 70% (vol/vol) ethanol. A midline incision of approximately 1 cm was made on the skin in the lower back, below the chest. The subcutaneous tissue was gently dissected to expose the muscular fascia, and the ovarian fat pad was identified under the muscular layer. The peritoneal cavity was cut with a 0.5-cm incision. The Fallopian tube was exposed, and the ovary identified and cut at the level of the oviduct. The blood vessels were cauterized to prevent bleeding. The remaining part of the Fallopian tube was placed

back in the peritoneal cavity, and the muscular fascia was sutured. The same protocol was repeated for the contralateral ovary. At the end, the skin was sutured. The animals received metamizole (Sanofi Aventis, no. Ay005, 200 mg per kg body weight during surgery) and meloxicam (Boehringer-Ingelheim, no. KPOEH3R, 5 mg per kg body weight subcutaneously after surgery every 24 h for 3 consecutive days), 2 mg per kg body weight subcutaneously after surgery. Animals were euthanized at P60.

Transcardiac perfusion

For histological analysis, animals were quickly anesthetized with isoflurane (Zoetis, no. 6089373) and secured to the perfusion plate. The chest was open to expose the heart. The left ventricle was cannulated and the inferior vena cava cut. Animals were initially perfused with 30 ml of PBS with heparin (100 mg l⁻¹; Sigma, no. H0878), followed by 30 ml of 4% (wt/vol) paraformaldehyde (Sigma, no. P6148) in PBS using a peristaltic pump (Behr, no. PLP 380, speed of 25 r.p.m.). Animals were decapitated, the brain explanted, fixed in 4% (wt/vol) paraformaldehyde for 30 min and post-fixed in 4% (wt/vol) PBS overnight (16 h). Then the tissues were washed in PBS and stored at 4 °C with 0.025% (wt/vol) sodium azide (VWR, no. 786-299). For cryoprotection, the tissue was transferred to 30% (wt/vol) sucrose (Sigma, no. 84097) in PBS and incubated overnight at 4 °C. To increase antibody permeability, the brain slices were frozen over dry ice and thawed at room temperature for three cycles.

Vibratome sections

Cryoprotected samples were embedded into 3% (wt/vol) agarose/PBS to obtain coronal brain sections. The brain was sliced in 100- μ m coronal sections on a vibratome (Leica VT 1200S).

Immunofluorescence staining

The brain slices were incubated in blocking solution containing 1% (wt/vol) BSA (Sigma, A9418), 5% (vol/vol) Triton X-100 (Sigma, T8787), 0.5% (wt/vol) sodium azide (VWR, 786-299) and 10% (vol/vol) serum (either goat, Millipore, no. S26, or donkey, Millipore, no. S30) for 1 h at room temperature on a shaker. Afterwards, the samples were immunostained with primary antibodies diluted in antibody solution containing 1% (wt/vol) BSA, 5% (vol/vol) Triton X-100, 0.5% (vol/vol) sodium azide, 3% (vol/vol) goat or donkey serum, and incubated for 48 h on a shaker at room temperature. The following primary antibodies were used: rat α -CD68 (AbD Serotec, no. MCA1957, clone FA-11; 1:250 dilution), goat α -Iba1 (Abcam, ab5076, FR3288145-1; 1:250 dilution) and rabbit anti-Iba1 (GeneTex, no. GTX100042, no. 41556, 1 vol/vol 750). The slices were then washed three times with PBS and incubated for 2 h at room temperature on a shaker protected from light, with the secondary antibodies diluted in antibody solution. The secondary antibodies raised in goat or donkey were purchased from Thermo Fisher Scientific (Alexa Fluor 488 goat anti-rabbit IgG no. A11034, Alexa Fluor 647 goat anti-rat IgG 21247; 1:2,000 dilution). The slices were washed three times with PBS. The nuclei were labeled with Hoechst 33342 (Thermo Fisher Scientific, no. H3570; 1:5,000 dilution) diluted in PBS for 15 min. The slices were mounted on microscope glass slides (Assistant, no. 42406020) with coverslips (Menzel-Glaser no. 0) using an antifade solution (10% (vol/vol) Mowiol (Sigma no. 81381), 26% (vol/vol) glycerol (Sigma, no. G7757), 0.2 M Tris buffer (pH 8) and 2.5% (wt/vol) Dabco (Sigma, no. D27802)).

Confocal microscopy

Images were acquired with a Zeiss LSM880 upright Airy scan or with a Zeiss LSM700 upright using a Plan-Apochromat \times 40 oil-immersion objective 1.4 NA. Then, 2 \times 2 z-stack tail images were acquired with a resolution of 1,024 \times 1,024 pixels.

Image processing

Confocal tile images were stitched using the software Imaris Stitcher 9.3.1.v. Then, the confocal images were loaded in Fiji 1.52e (<http://>

imagej.net/Fiji). To remove the background, the rolling ball radius was set to 35 pixels, and images were filtered using a median 3D filter with x , y and z radii set at 3. Image stacks were exported as .tif files, converted to .ims files using the Imaris converter and imported into Imaris 8.4.2.v. (Bitplane Imaris).

Quantification of CD68 volume within cells

Surface renderings were generated on microglia and CD68 z-stacks using the surface-rendering module of Imaris 9.2.v Surfaces were generated with the surface detail set to 0.2 μm . To determine the CD68 surface within microglia, the surface–surface coloc plugin was used. This analysis was performed on the entire image. The total ratio of CD68 volume within microglial volume (CD68-to-microglial volume) was calculated per image. To compute the CD68 fold change, the total CD68-to-microglial volume from each condition (sex/time point) was scaled to the CD68-to-microglial volume ratio from the respective adult control brain region. CD68 fold change > 1 means an increase in CD68 volume, while CD68 < 1 means a decrease in CD68 volume. CD68 fold change = 1 denotes no change in CD68 volume.

Quantification of microglia density and statistical analysis

The spot-function plugin of Imaris 9.2.v was used to count the number of cells, that is, the soma of iba1-positive microglia within every confocal image. Microglial cell density was estimated as the total number of cells obtained in this way, divided by the size of the imaged sample in mm^2 .

Reconstruction of 3D-traced microglia

After filtering and background subtraction, images were imported in Imaris 9.2.v (Bitplane Imaris). Microglial processes were traced in 3D with the filament-tracing plugin. Because the filament-tracing plugin provides a semiautomated reconstruction, this eliminates the need for a user-blind approach for selecting representative microglia. New starting points were detected when the largest diameter was set to 12 μm and with seeding points of 1 μm . Disconnected segments were removed with a filtering smoothness of 0.6 μm . After the tracing, we manually removed cells that were sitting at the border of the image and were only partially traced so that these cells would not be analyzed. The generated skeleton images were converted from .ims format (Imaris) to .swc format⁷³ by first obtaining the 3D positions (x , y and z) and the diameter of each traced microglial process using the ImarisReader toolbox for MATLAB (<https://github.com/PeterBeemiller/ImarisReader/>) and then exporting for format standardization using the NL Morphology Converter (<http://neuroland.org/>). Artifacts from the 3D reconstructions automatically failed to be converted into .swc format.

Analysis of morphometric features

Classic morphometric features were calculated from the .swc files using the functions Length (for total process length), N_branch (for number of branches), N_bifs (for number of branching points) and N_tips (for number of terminal points) from L-measure⁷⁴ (<http://cng.gmu.edu:8080/Lm/>).

Sholl analysis

Sholl curves were calculated from the .swc files using the sholl_crossings function of the NeuroM Python toolkit (<https://github.com/BlueBrain/NeuroM>). In brief, concentric Sholl spheres centered on the soma of a given traced microglia are constructed with a given step size radius. The number of microglial processes that intersect each Sholl sphere are determined. This step is performed for each traced microglia in the data. From this, Sholl curves of a microglial population are then calculated as the average number of intersections across the population.

Topological morphology descriptor

A topological data analysis algorithm, the TMD, was used to extract topological phenotypes, called persistence barcodes, from 3D

morphological structures (<https://github.com/BlueBrain/TMD/>;¹⁴). In brief, the 3D-reconstructed microglia is represented as a tree T rooted in its soma. The TMD summarizes this tree by calculating ‘persistence barcodes’, where each bar represents a persistent microglial process with respect to a filtering function, that is, the radial distance from the soma. Note that the persistence barcode that the TMD associates with T under this filtering function is invariant under rotations about the root and rigid translations of T in R^3 .

Each bar is described by two numbers: the radial distance, d_i , at which a process originates; and the distance, b_i , when it merges with a larger, more persistent process or with the soma. A bar can be equivalently represented as a point (d_i, b_i) in a ‘persistence diagram’. We could therefore convolve each point in the persistence diagram with a Gaussian kernel and discretize it to generate a matrix of pixel values, encoding the persistence diagram in a vector, called the ‘persistence image’.

Average and bootstrapped persistence images

To construct the ‘average persistence image’ of a given condition, all the persistence barcodes of microglia from the same condition are combined before Gaussian convolution and discretization are performed. We also constructed average persistence images by performing first the Gaussian convolution and discretization of individual microglia persistence barcodes before taking the pixel-wise average. This produced qualitatively similar results.

The bootstrapping method subsamples the microglial population within a given condition, thereby introducing variations around the average persistence image. Starting from the population of all microglia from the same condition, called the ‘starting population’ of size n (Supplementary Table 4), the persistence barcodes of a predefined number of unique microglia, called the ‘bootstrap size’, are combined to calculate the ‘bootstrapped persistence image’. We iterated this process a predefined number of times, n_{samples} , with replacement to obtain the ‘bootstrap sample’.

Subtraction images and topological morphology descriptor distance

The subtraction image is the pixel-wise difference between two given persistence images. From the subtraction image, the TMD distance can be computed as the sum of the absolute pixel-wise difference. For stability of the TMD distance, we refer the reader to Kanari et al.¹⁴.

Hierarchical clustering

Hierarchical clustering allowed us to find similarities between microglia across several conditions. Hierarchical clustering was done on the basis of the average persistence images. Clusters were then identified hierarchically using the average linkage criterion with the TMD distance metric and was implemented using cluster.hierarchy.linkage from SciPy v1.6.2 (<https://www.scipy.org/>). Dendrograms were generated using cluster.hierarchy.dendrogram to visualize the arrangement of the resulting cluster.

Dimensionality reduction

Uniform manifold approximation and projection. A fast, nonlinear dimensionality reduction algorithm, UMAP⁷⁵, was applied to visualize the high-dimensional pixel space of bootstrapped persistence images using a 2D representation while preserving local and global structures in the bootstrap samples (<https://github.com/lmcinnes/umap/>)⁷⁵. Given a bootstrap sample containing multiple conditions, a TMD distance matrix containing pairwise distances between bootstrapped persistence images in the bootstrap sample is calculated. Principal components are then obtained using a singular value decomposition of the TMD distance matrix. The first seven principal components, where the elbow in the singular values is located, were used as input to UMAP with $n_{\text{neighbors}} = 50$, $\text{min_dist} = 1.0$ and $\text{spread} = 3.0$. Note that we tested for a wide range of parameter values that did not

qualitatively change any of the aforementioned observations (Extended Data Fig. 2f).

***t*-SNE.** An alternative dimensionality reduction algorithm is *t*-SNE (<https://github.com/DmitryUlyanov/Multicore-TSNE/>), which finds a dimensionality-reduced representation where similar points are pulled closer together while dissimilar points are pushed farther apart with high probability. The first seven principal components were taken as an input to run *t*-SNE with perplexity = 50.

Pseudo-temporal ordering. The concept of morphological phenotypes as encoded in the persistence images can be likened to transcriptional phenotypes in single-cell RNA-sequencing studies. Bootstrapped persistence images, which encapsulate morphological phenotypes of microglial populations from similar conditions, are comparable. Furthermore, it is reasonable to assume that morphological changes in bootstrapped microglial populations from control-to-disease conditions occur with incremental differences in the persistence images. This conceptual similarity allowed us to use the pseudo-temporal trajectory-inference algorithms that are well used in the single-cell RNA-sequencing community to study the morphological progression during microglial development and degeneration.

Palantir. Palantir⁷⁶ uses principles from graph theory and Markov processes to calculate the pseudo-time and the probability of a cell reaching each of the terminal conditions in the sample (<https://github.com/dpeerlab/Palantir/>). First, the principal components of the bootstrapped persistence images were obtained using `palantir.utils.run_pca` with `n_components = 100` and `use_hvg = false`. The diffusion maps were then calculated from the PCA projections using `palantir.utils.run_diffusion_maps` with `n_components = 10` and `knn = 20` which outputs the Palantir pseudo-times. Harmony⁷⁷ was then used to construct an augmented affinity matrix from the Palantir pseudo-times to connect the Palantir pseudo-times and construct a trajectory using a force-directed graph (<https://github.com/dpeerlab/Harmony/>).

Monocle. To corroborate the Palantir trajectories, an alternative pseudo-temporal trajectory-inference algorithm called Monocle was used. Monocle⁷⁸ uses reversed graph embedding, which learns a principal graph that approximates a lower-dimensional manifold to construct a pseudo-time trajectory (<https://github.com/cole-trapnell-lab/monocle3/>)⁷⁸. Similar to Palantir implementation, the principal components of the bootstrapped persistence images were first obtained using `preprocess_cds` with `num_dim = 100`. A 2D UMAP representation was then obtained using `reduce_dimension` with `umap.metric = 'manhattan'`, `umap.min_dist = 1.0`, and clusters were identified using `cluster_cells` with `cluster_method = 'leiden'`. Finally, the pseudo-temporal trajectory was then obtained using `learn_graph` with `use_partition = FALSE` and `close_loop = FALSE`.

Stable ranks analysis. An alternative representation of the persistence barcodes is through stable ranks⁷⁹. Stable ranks are functional summaries of persistence that depend on pseudometrics to compare persistence barcodes. Given a pseudometric d , the stable rank $\widehat{\text{rank}}_d(X)(t)$ of a persistence barcode X is a function that assigns to t the number:

$$\widehat{\text{rank}}_d(X)(t) = \min \{ \text{rank}(Y) \mid d(Y, X) \leq t \}.$$

whereby ' $\text{rank}(Y)$ ' denotes the number of bars of the persistence barcode Y . The stable rank $\widehat{\text{rank}}_d(X)(t)$ associates to a persistence barcode a non-increasing and piece-wise constant function with values in $[0, \infty)$. An important property is that this mapping is continuous with respect to the chosen pseudometric d and the L_p metric on the space \mathcal{M} of measurable functions.

A class of pseudometrics on persistence barcodes can be constructed from density functions⁷⁹, which intuitively are used to vary

the weight along the filtration scale parametrizing a barcode. With such pseudometrics, the stable rank is a bar count based on length of bars as scaled by the density. The standard stable rank is defined by a density function with constant value one. In this case, $\widehat{\text{rank}}_d(X)(t)$ is the number of bars in X with length greater than or equal to t , that is, all filtration scales are weighted equally.

Stable ranks can be used in place of persistence images in the MorphOMICs pipeline. Similarly to MorphOMICs, the persistence barcode X of a given microglia is calculated using the TMD algorithm. To obtain 'bootstrapped standard stable ranks', we combined the persistence barcodes of a predefined number of microglia and computed their standard stable ranks. Dimensionality reduction was then implemented similar to the methods above ('Dimensionality reduction').

Classification accuracy using stable ranks. To support and quantify the impact of bootstrapping on the regional segregation visualized in the reduced UMAP space (Fig. 1f), we performed a classification task for microglia morphologies represented by their standard stable rank and labeled by brain region. We used an SVM with a specific kernel based on stable ranks^{80,81} for the classification. For persistence barcodes X and Y , the stable rank kernel with respect to a pseudometric d is given by

$$K_d(X, Y) = \int_0^{\infty} \widehat{\text{rank}}_d(X)(t) \widehat{\text{rank}}_d(Y)(t) dt.$$

where we used the pseudometric induced by the constant function with value one.

We performed pairwise classifications. For each pair of brain regions, we constructed a dataset consisting of 400 bootstrap samples, that is, 200 from each region and bootstrap sizes of 10, 20 or 50 (the results are reported separately for these three values). We randomly partitioned the dataset for cross-validation wherein 240 samples were used for SVM training (training set) and 160 samples for validation (test set). We reported the average accuracy over ten repeated cross-validations on the test set. The SVM was trained using the implementation in the Python library `sklearn` (<https://scikit-learn.org/stable/>) with default settings except for the usage of the stable rank kernel.

Bootstrapped morphometric features and bootstrapped Sholl curves. To understand whether classical morphology analysis pipelines are able to recapitulate the microglial dynamics recovered by MorphOMICs, a similar bootstrapping analysis was also done where we pooled a predefined number of microglia. Each morphometric quantity in the extended list enumerated in Supplementary Table 3 was then averaged to obtain a 27-dimensional vector, with each dimension corresponding to a morphometric feature, called the 'bootstrapped morphometric features'. On the other hand, Sholl curves averaged across the pooled microglia to obtain the 'bootstrapped Sholl curves'. Dimensionality reduction was then implemented similarly to the methods above ('Dimensionality reduction').

Mapping morphologies onto the reference atlas. We have generated a larger reference atlas with $n_{\text{samples}} = 2,000$ bootstrapped persistence images for each condition to construct the Palantir trajectories. Palantir coordinates (x, y) were rescaled to $(0, 1)$. We took and filtered the bootstrapped persistence images keeping only the 500 most highly variable pixels across the images in all conditions. We used linear regression, one for each axis, to learn the mapping from the filtered bootstrapped persistence image to the rescaled Palantir coordinates. Given a novel condition, we generated the bootstrapped persistence images and filtered them with the 500 most highly variable pixels identified earlier. We used the trained regression model to infer the locations of each image in the reference atlas. Then, we calculated the mean position denoting the center of the inferred locations and indicated the spread using the standard deviation.

Statistics and reproducibility

Each experiment was repeated independently with similar results. Supplementary Table 4 provides the numbers of 3D traces obtained per condition, sex and brain region. Supplementary Table 5 describes the number of animals per condition, their sex and brain region.

In Extended Data Figs. 1a and 10a, statistical analysis was performed using `scipy.stats` (v1.6.2) and `scikit-posthocs` (v0.6.7). These morphometric features were first tested for normality using the Kolmogorov–Smirnov test (`scipy.stats.kstest`). After determining the non-normal distribution of the features, we performed non-parametric pairwise tests for independence between measurements from two brain regions using the Kruskal–Wallis test (`scipy.stats.kruskal`). We used Bonferroni-corrected *P* values, calculated using Dunn's test via `scikit_posthocs.posthoc_dunn` (Supplementary Table 1).

In Extended Data Fig. 4a,b, statistical analysis was performed using R (v3.4.4). Normality of the microglial average densities was tested using Shapiro–Wilk's test (`shapiro.test()`). Differences in densities were compared with two-sided *t*-test. When comparing between brain regions, Tukey's post hoc test (`TukeyHSD()`) was used for multiple comparisons (Supplementary Table 2).

Reporting summary

Further information on research design is available in the Nature Research Reporting Summary linked to this article.

Data availability

The .swc files generated during the current study are available in the [NeuroMorpho.org](https://neuro-morpho.org) repository in the Siegert archive at <https://neuro-morpho.org/KeywordResult.jsp?keywords=%22siegert%22>. Source data are provided with this paper.

Code availability

The codes and the reference atlas are available to download on GitHub (<https://git.ist.ac.at/rcubero/morphomics/>), with detailed instructions on implementation.

References

69. Cruz, J. C., Tseng, H. C., Goldman, J. A., Shih, H. & Tsai, L. H. Aberrant Cdk5 activation by p25 triggers pathological events leading to neurodegeneration and neurofibrillary tangles. *Neuron* **40**, 471–483 (2003).
70. Erny, D. et al. Host microbiota constantly control maturation and function of microglia in the CNS. *Nat. Neurosci.* **18**, 965–977 (2015).
71. Venturino, A. & Siegert, S. Minimally invasive protocols and quantification for microglia-mediated perineuronal net disassembly in mouse brain. *STAR Protoc.* **2**, 101012 (2021).
72. Lein, E. S. et al. Genome-wide atlas of gene expression in the adult mouse brain. *Nature* **445**, 168–176 (2006).
73. Stockley, E., Cole, H., Brown, A. & Wheal, H. A system for quantitative morphological measurement and electronic modelling of neurons: three-dimensional reconstruction. *J. Neurosci. Methods* **47**, 39–51 (1993).
74. Scorcioni, R., Polavaram, S. & Ascoli, G. A. L-Measure: a web-accessible tool for the analysis, comparison, and search of digital reconstructions of neuronal morphologies. *Nat. Protoc.* **3**, 866–876 (2008).
75. McInnes, L., Healy, J. & Melville, J. UMAP: uniform manifold approximation and projection for dimension reduction. Preprint at <https://arxiv.org/abs/1802.03426> (2018).
76. Setty, M. et al. Characterization of cell fate probabilities in single-cell data with Palantir. *Nat. Biotechnol.* **37**, 451–460 (2019).
77. Nowotschin, S. et al. The emergent landscape of the mouse gut endoderm at single-cell resolution. *Nature* **569**, 361–367 (2019).

78. Cao, J. et al. The single-cell transcriptional landscape of mammalian organogenesis. *Nature* **566**, 496–502 (2019).
79. Riihimäki, H. & Chacholski, W. Generalized persistence analysis based on stable rank invariant. Preprint at <https://arxiv.org/abs/1807.01217> (2018).
80. Agerberg, J., Ramanujam, R., Scolamiero, M. & Chacholski, W. Supervised learning using homology stable rank kernels. *Front. Appl. Math. Stat.* **7**, 668046 (2021).
81. Polavaram, S., Gillette, T. A., Parekh, R. & Ascoli, G. A. Statistical analysis and data mining of digital reconstructions of dendritic morphologies. *Front. Neuroanat.* **8**, 138 (2014).

Acknowledgements

We thank the scientific service units at ISTA, in particular M. Schunn's team at the preclinical facility, and especially our colony manager S. Haslinger, for excellent support. We are also grateful to the ISTA Imaging & Optics Facility, and in particular C. Sommer for helping with the data file conversions. We thank R. Erhart from the ISTA Scientific Computing Unit for improving the script performance. We thank M. Maes, B. Nagy, S. Oakeley and M. Benevento and all members of the Siegert group for constant feedback on the project and on the manuscript. This research was supported by the European Union Horizon 2020 research and innovation program under the Marie Skłodowska-Curie Actions program (754411 to R.J.A.C.), and by the European Research Council (grant no. 715571 to S.S.). L.K. was supported by funding to the Blue Brain Project, a research center of the École polytechnique fédérale de Lausanne, from the Swiss government's ETH Board of the Swiss Federal Institutes of Technology. L.-H.T. was supported by NIH (grant no. R37NS051874) and by the JPB Foundation. The funders had no role in study design, data collection and analysis, decision to publish or preparation of the manuscript.

Author contributions

Conceptualization, G.C., R.J.A.C., L.K., M.S., J.A., W.C., K.H. and S.S.; methodology, G.C., R.J.A.C., L.K. and S.S.; software, R.J.A.C. and L.K.; validation, G.C. and R.J.A.C.; formal analysis, G.C., R.J.A.C. and L.K.; investigation, G.C., R.J.A.C., A.V., R.S. and S.S.; resources, L.K., H.M. and L.-H.T.; data curation, G.C. and R.J.A.C.; writing—original draft and visualization, G.C., R.J.A.C. and S.S.; supervision, project administration and funding acquisition, S.S.; stable ranks: conceptualization, G.C., R.J.A.C., L.K., M.S., J.A., W.C., K.H. and S.S.; software validation and formal analysis, R.J.A.C. and J.A.

Competing interests

The authors declare no competing interests.

Additional information

Extended data is available for this paper at <https://doi.org/10.1038/s41593-022-01167-6>.

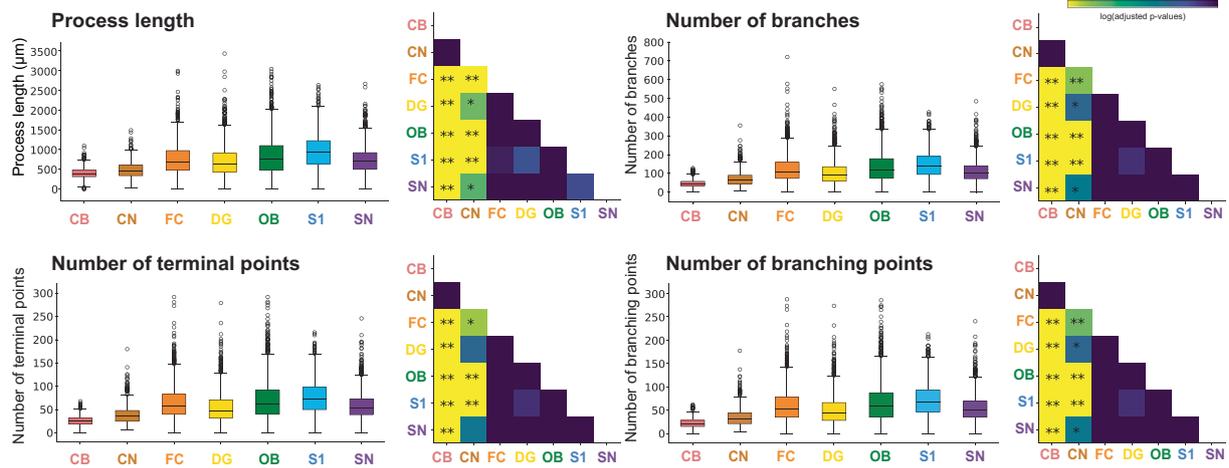
Supplementary information The online version contains supplementary material available at <https://doi.org/10.1038/s41593-022-01167-6>.

Correspondence and requests for materials should be addressed to Sandra Siegert.

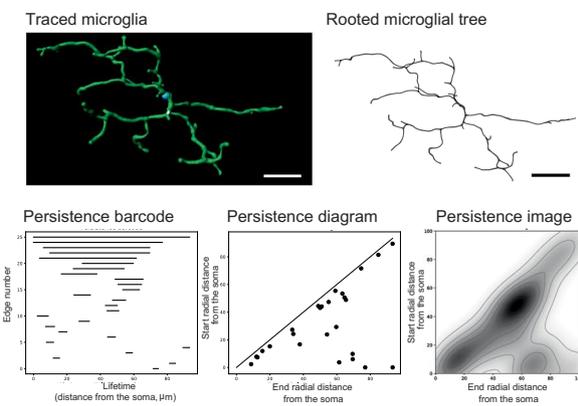
Peer review information *Nature Neuroscience* thanks Giorgio Ascoli, Michael Salter, and the other, anonymous, reviewer(s) for their contribution to the peer review of this work.

Reprints and permissions information is available at www.nature.com/reprints.

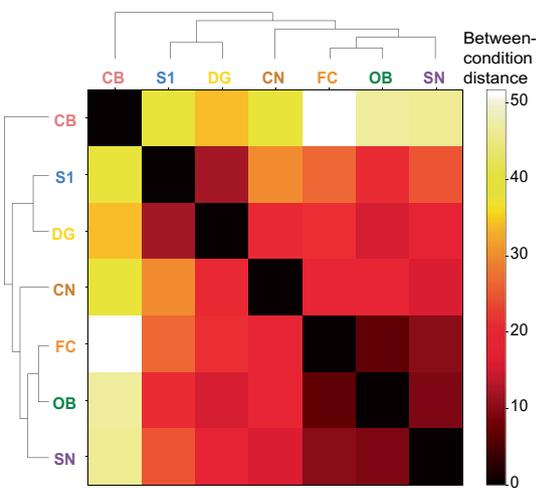
A Common morphometric classifiers



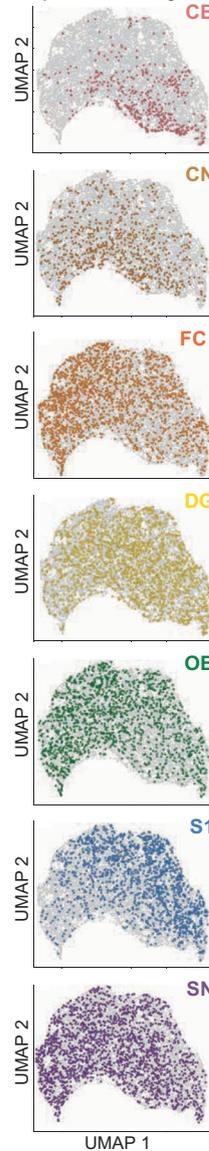
B Conversion with a representative microglial morphology



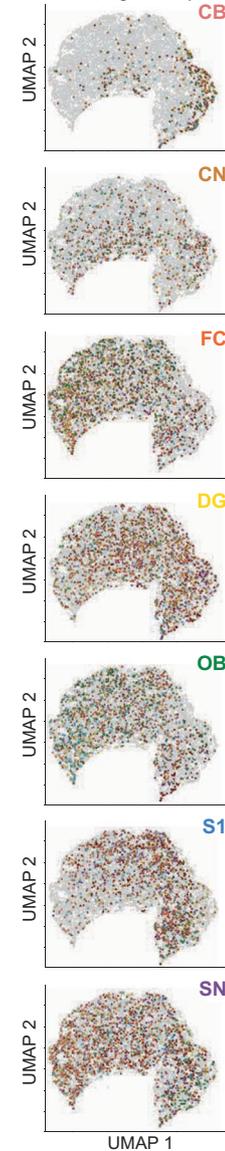
C TMD: Distance matrix



D TMD: Intrinsic spatial heterogeneity



E TMD: Distribution of the biological triplicate



Extended Data Fig. 1 | See next page for caption.

Extended Data Fig. 1 | Classic morphometry analysis and intrinsic variability of microglial morphology. **a:** Box plots for the following morphometric features: process length, number of branches, and terminal and branching points for traced adult C57BL/6J microglia across different brain regions color-coded: CB (cerebellum, $n = 299$), CN (cochlear nucleus, $n = 498$), FC (frontal cortex, $n = 926$), DG (dentate gyrus, $n = 902$), OB (olfactory bulb, $n = 796$), S1 (somatosensory cortex, $n = 719$), SN (substantia nigra, $n = 1050$) from at least six animals. For number of animals per condition and region see also Supplementary Table 5. Box denotes first and last quartile with central line indicating the median. Whiskers: range of quantities. Open circle: outliers. Next, matrices with color-coded p -values for the pairwise comparison of each morphometric. Kruskal-Wallis test, Bonferroni correction using Dunn's test, * $p < 0.05$, ** $p < 0.01$ (see

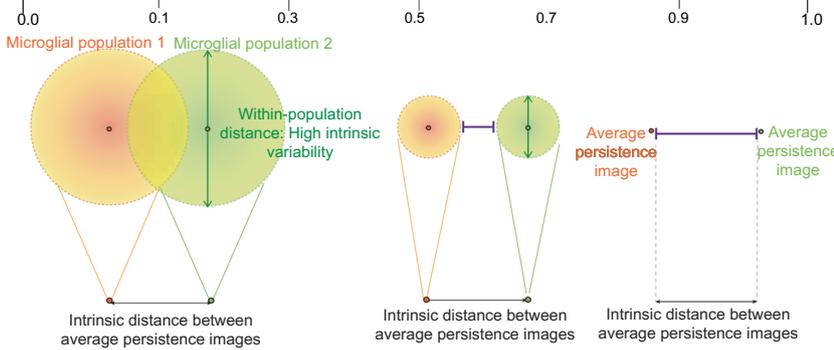
Supplementary Table 1, 3). **b:** Example of a 3D-traced microglia and its conversion to a persistence image. Top: left, Imaris-traced skeleton of a microglia. Scale bar: $10 \mu\text{m}$. Right, formatted rooted microglia tree, which is used for the persistence plots. Bottom: persistence barcode (left), persistence diagram (middle), and persistence image (right) exactly matching the rooted tree. **c:** Hierarchically-ordered heat map for pairwise TMD intrinsic distances between average persistence images from microglia across brain regions from Fig. 1a. **d-e:** UMAP plots of the entire microglial population size (grey) with color-highlighted brain regions (**d**) or animals (**e**). Each dot represents a single persistence image. (**e**) Triangle and circle for females and males, respectively. Each animal is color-coded.

A MorphOMICs:

Bootstrap and variability reduction

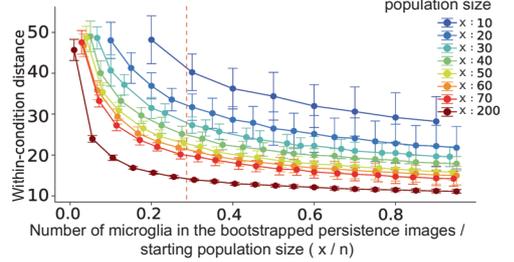
Microglial bootstrap to population size ratio (x/n)

(Ratio between the number of microglia in the bootstrapped persistence images x and the starting population size n)

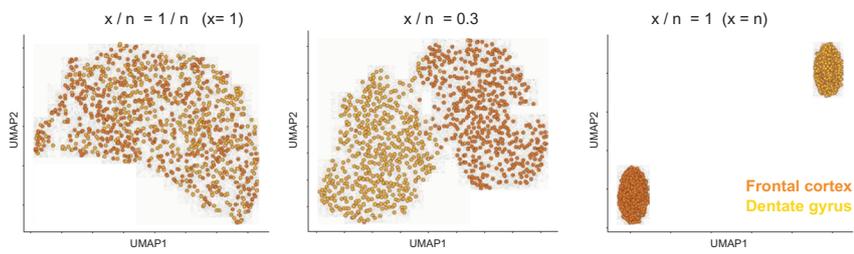


C

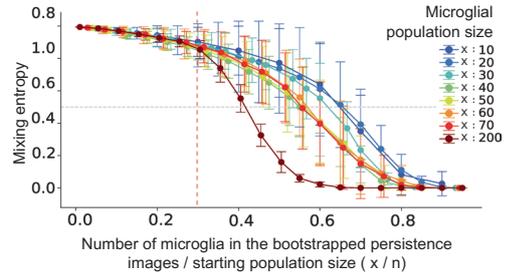
Within-population distance



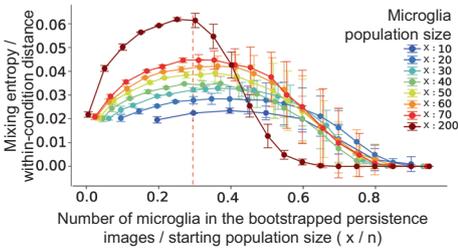
B Data segregation for different bootstrap (x)-to-population size (n)



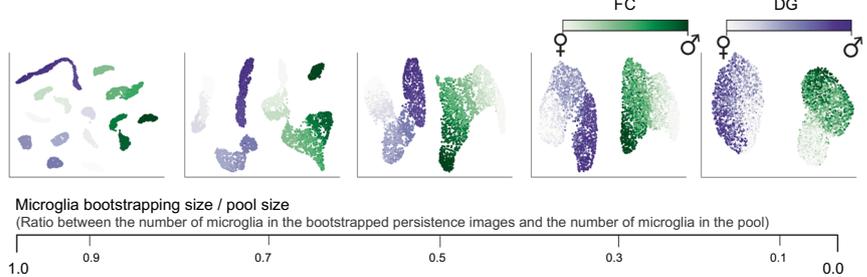
Mixing entropy



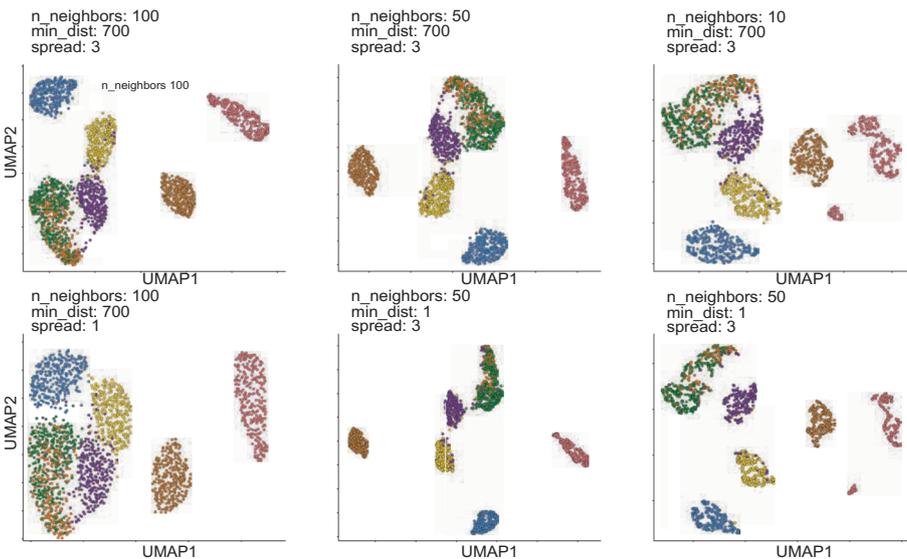
D Mixing entropy and within-condition distance



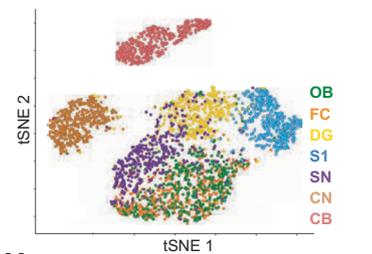
E Female/male ratio



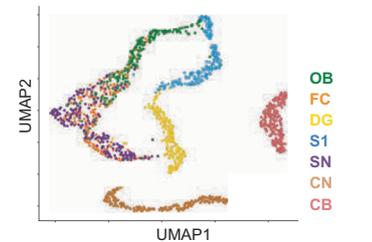
F UMAP hyperparameters



G tSNE



H Stable ranks

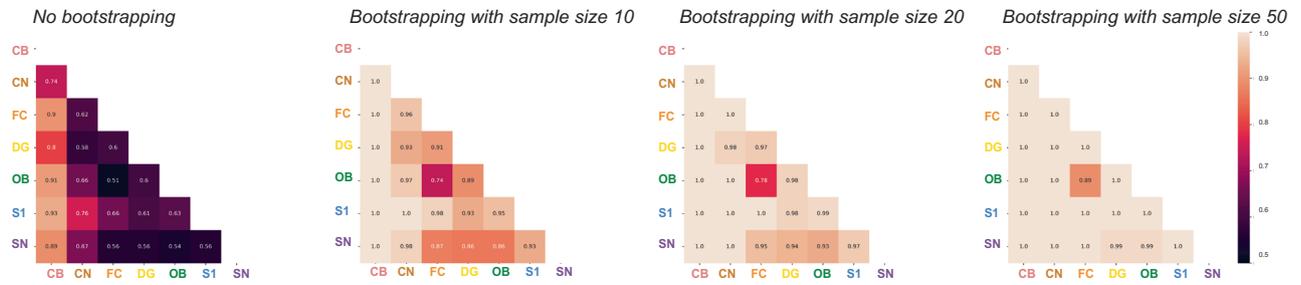


Extended Data Fig. 2 | See next page for caption.

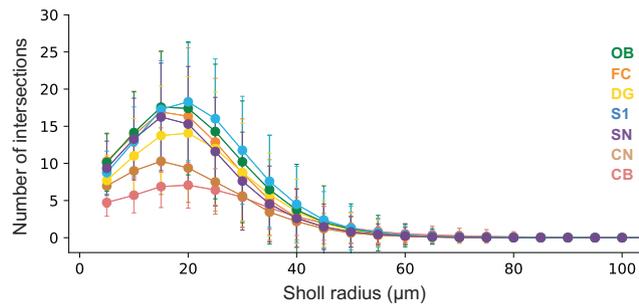
Extended Data Fig. 2 | Details about the MorphOMICS paradigm. a: Schematic of the bootstrapping effects on the distance between tree structures from the same population (within-population distance, green arrows) and two distinct populations (distance between average persistence images, purple lines). Increase of bootstrap-to-population size ratio (x/n) reduces within-population distance and increases distance between average persistence images. **b:** UMAP plots of MorphOMICS-analyzed microglia for frontal cortex (orange) and dentate gyrus (yellow) for different bootstrap-to-population size ratios. Left: $x = 1$, allows no segregation. Middle: $x/n = 0.3$. Right: $x/n = 1$ causes accentuation. **c, d:** Line plot \pm SD displays how within-population distance (**c**, top) and mixing entropy (**c**, bottom), and the ratio between mixing entropy and within-condition distance (**d**) varies by enhancing bootstrap-to-population size ratio (x/n). An empirical threshold of 0.3 was selected (red dashed line). Data are presented as mean

values \pm SD. **e:** UMAP plots of MorphOMICS-analyzed microglia for frontal cortex (green) and dentate gyrus (purple) for different bootstrap-to-population size ratios and varying male-to-female ratios within the population size. **f:** UMAP plots of MorphOMICS-analyzed microglial morphology across seven brain regions as shown for Fig. 1f with examples of tested hyperparameters for number of neighbors ($n_neighbors$), minimum distance (min_dist), and spread. Olfactory bulb (OB), frontal cortex (FC), dentate gyrus (DG), somatosensory cortex (S1), substantia nigra (SN), cochlear nucleus (CN), and cerebellum (CB). **g:** tSNE plot of MorphOMICS-analyzed microglia across seven brain regions as shown in Fig. 1f. **h:** UMAP plots of stable ranks representation of microglial morphology (see Methods: *Stable Ranks*) across seven brain regions. $n_{samples} = 500$ per condition (see also Methods: *Average and bootstrapped persistence images*). SD: standard deviation.

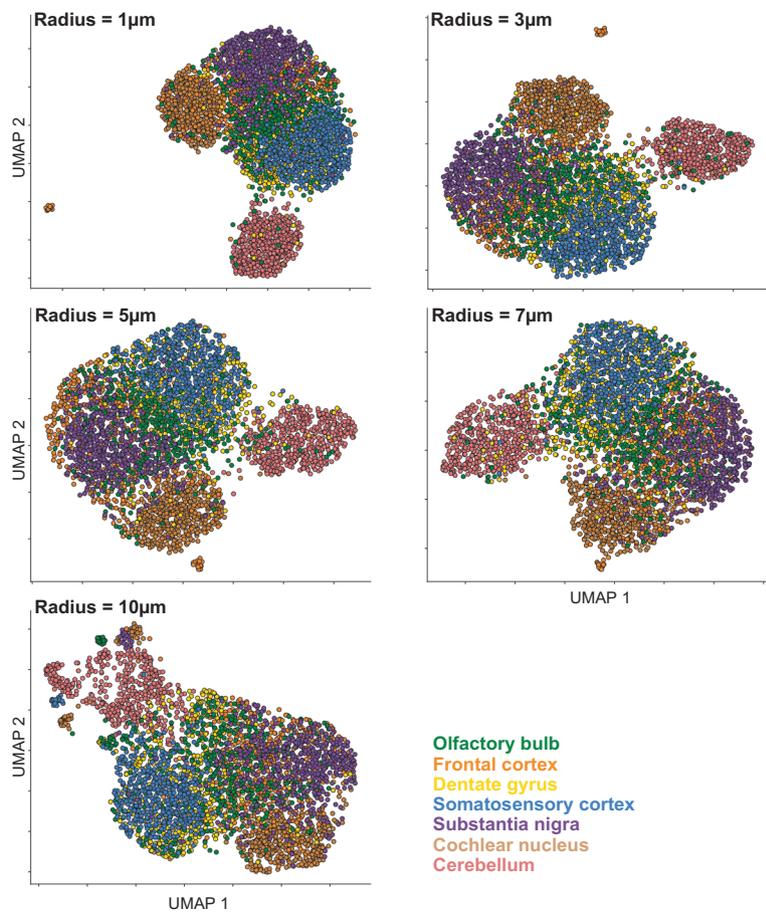
A Classification accuracy of microglial morphology with stable ranks



B Sholl analysis to describe microglial morphology



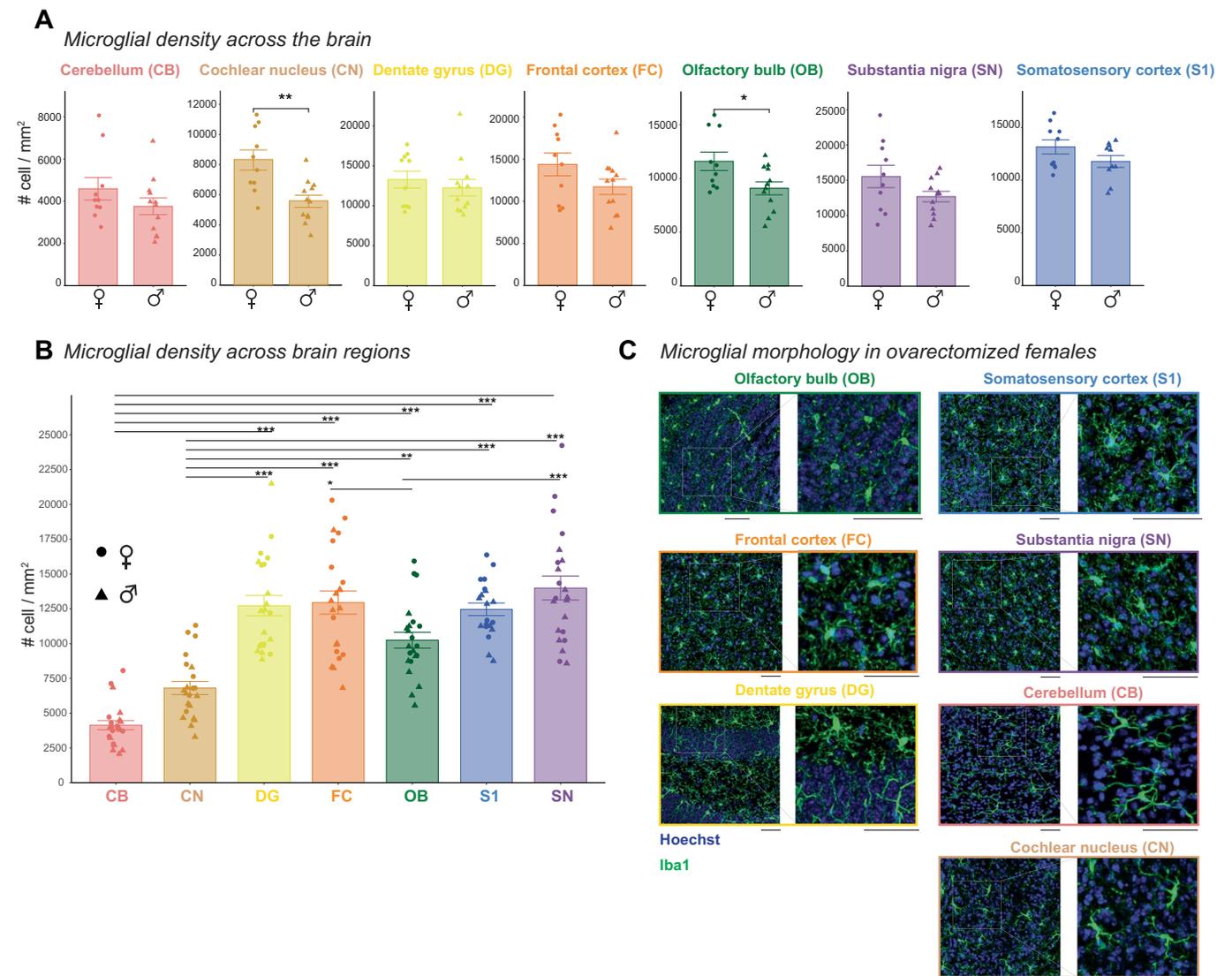
C Bootstrap application on Sholl analysis



Extended Data Fig. 3 | See next page for caption.

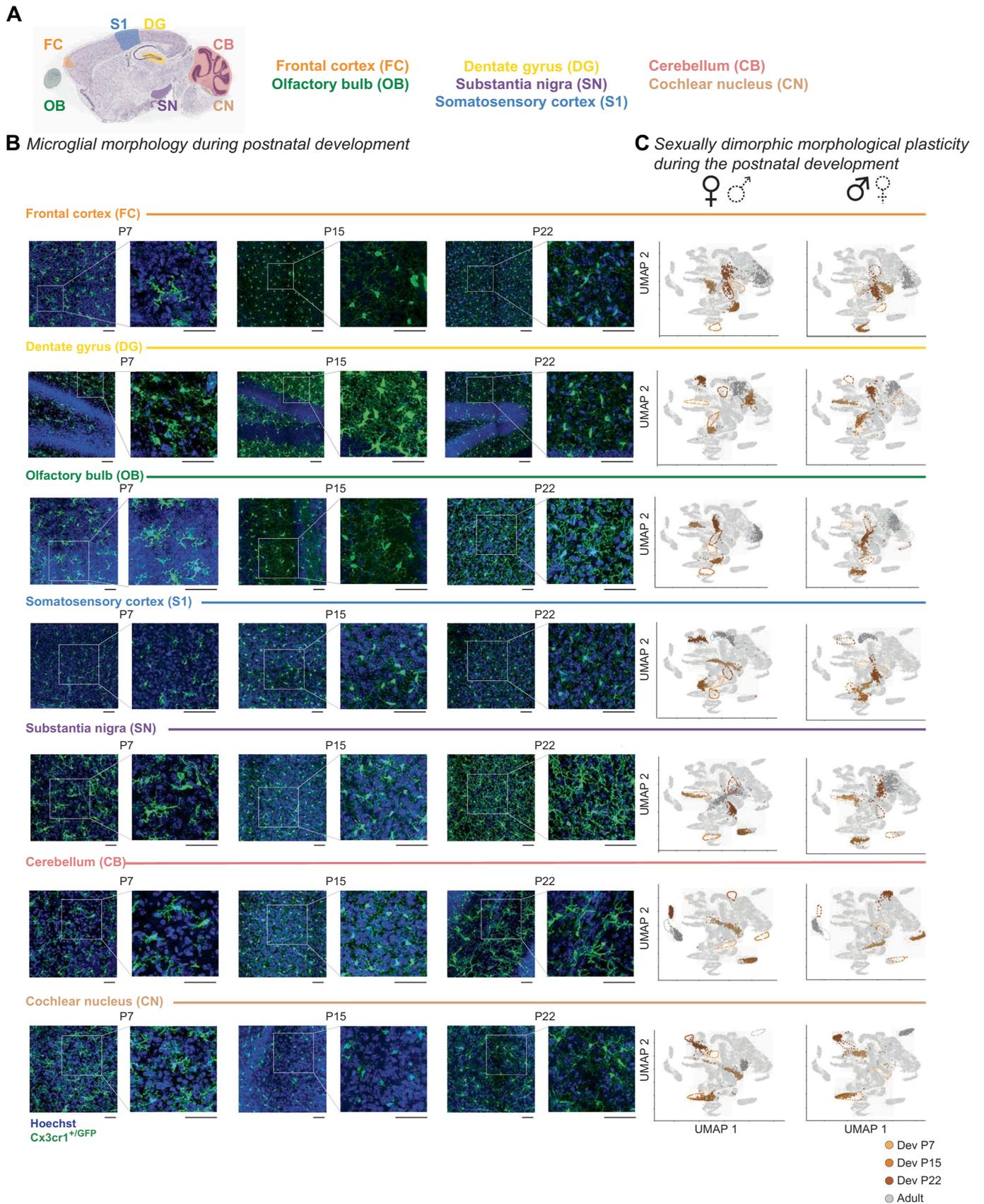
Extended Data Fig. 3 | Classification accuracy of microglial morphology and bootstrap application on Sholl analysis. a: Heat-map of classification accuracy between pairs of brain regions using stable ranks for different bootstrap sizes. Numbers indicates the percentage of microglia correctly assigned in the classification task, averaged over 10 repeated cross-validations. 1, perfect assignment; 0.5 random assignment. **b:** Sholl curves for each brain region. Data are presented as mean number of processes (points) \pm SD that intersect with a series of concentric Sholl spheres centered on the soma and spaced at 5 μm . For

number of animals per condition and region see Supplementary Table 4, 5. **c:** Bootstrapped and UMAP visualized Sholl-analyzed microglia, color-coded for each brain region. Each dot represents a bootstrapped Sholl analysis. Each plot has a set radius step size (1, 3, 5, 7, 10 μm). Olfactory bulb (OB), frontal cortex (FC), dentate gyrus (DG), somatosensory cortex (S1), substantia nigra (SN), cochlear nucleus (CN), and cerebellum (CB). $n_{\text{samples}} = 300$ per condition (see also Methods: *Average and bootstrapped persistence images*). SD: standard deviation.



Extended Data Fig. 4 | Adult microglial density and microglial morphologies after ovariectomy. a-b: Bar plot of microglial density distribution for each brain regions in C57BL/6J female and male adults. Data are presented as mean number of cells per $\text{mm}^2 \pm \text{SD}$. After determining normal distribution of the features with Shapiro-Wilk test, (a) sex averages for microglia from each region were compared with two-sided t-test. Each dot represents one animal. $\text{CN}_{\text{mg}} (n_{\text{f}}=10, n_{\text{m}}=12)$: $t = 3.504$, $\text{df} = 15.1$, $p\text{-value} = 0.00312$. $\text{OB}_{\text{mg}} (n_{\text{f}}=10, n_{\text{m}}=12)$: $t = 2.401$, $\text{df} = 16.864$, $p\text{-value} = 0.0282$. $\text{CB}_{\text{mg}} (n_{\text{f}}=10, n_{\text{m}}=12)$: $t = 1.2564$, $\text{df} = 17.327$, $p\text{-value} = 0.2257$. $\text{FC}_{\text{mg}} (n_{\text{f}}=10, n_{\text{m}}=12)$: $t = 1.6236$, $\text{df} = 16.275$, $p\text{-value} = 0.1237$. $\text{SN}_{\text{mg}} (n_{\text{f}}=10, n_{\text{m}}=12)$: $t = 1.6261$, $\text{df} = 12.901$, $p\text{-value} = 0.1281$. $\text{DG}_{\text{mg}} (n_{\text{f}}=10, n_{\text{m}}=12)$: $t = 0.68892$, $\text{df} = 19.669$, $p\text{-value} = 0.4989$. $\text{S1}_{\text{mg}} (n_{\text{f}}=10, n_{\text{m}}=12)$: $t = 1.5618$, $\text{df} = 17.518$, $p\text{-value} = 0.1362$. SD: standard deviation. * $p < 0.05$, ** $p < 0.01$. (b) Analysis of variance (ANOVA) on densities yielded significant variation among conditions, $F = 17.98$, $p < .001$.

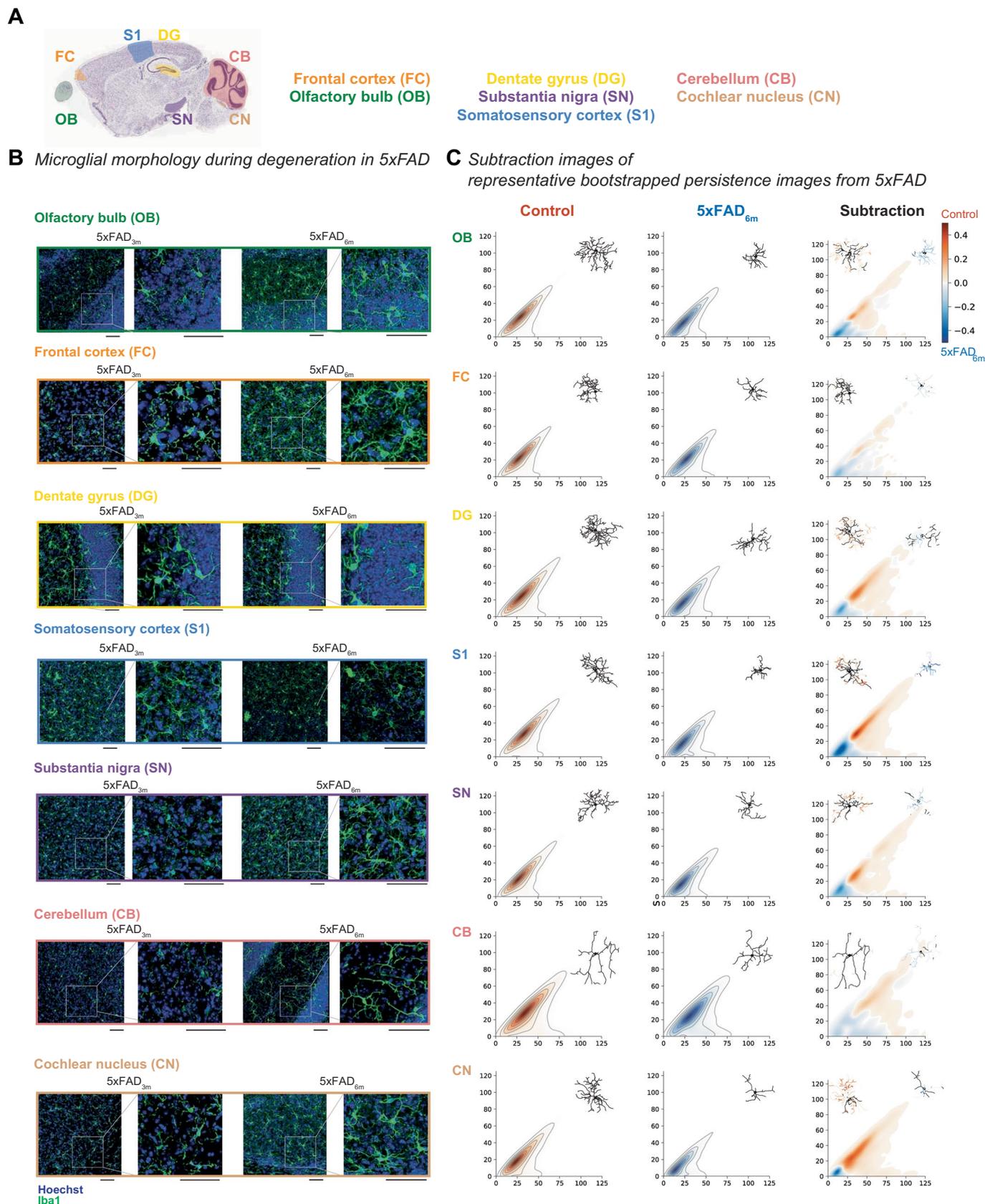
$F = 33.35$, $p < .001$. Tukey post hoc test was computed for pairwise comparisons. $(\text{CN}-\text{CB})p.\text{adj} = 0.0523543$; $(\text{DG}-\text{CB})p.\text{adj} = 0.0000000$; $(\text{FC}-\text{CB})p.\text{adj} = 0.0000000$; $(\text{OB}-\text{CB})p.\text{adj} = 0.0000000$; $(\text{S1}-\text{CB})p.\text{adj} = 0.0000000$; $(\text{SN}-\text{CB})p.\text{adj} = 0.0000000$; $(\text{DG}-\text{CN})p.\text{adj} = 0.0000000$; $(\text{FC}-\text{CN})p.\text{adj} = 0.0000000$; $(\text{OB}-\text{CN})p.\text{adj} = 0.0036669$; $(\text{S1}-\text{CN})p.\text{adj} = 0.0000002$; $(\text{SN}-\text{CN})p.\text{adj} = 0.0000000$; $(\text{FC}-\text{DG})p.\text{adj} = 0.9999824$; $(\text{OB}-\text{DG})p.\text{adj} = 0.0898840$; $(\text{S1}-\text{DG})p.\text{adj} = 0.9999557$; $(\text{SN}-\text{DG})p.\text{adj} = 0.7953985$; $(\text{OB}-\text{FC})p.\text{adj} = 0.0474778$; $(\text{S1}-\text{FC})p.\text{adj} = 0.9985099$; $(\text{SN}-\text{FC})p.\text{adj} = 0.9051447$; $(\text{S1}-\text{OB})p.\text{adj} = 0.1998237$; $(\text{SN}-\text{OB})p.\text{adj} = 0.0009832$; $(\text{SN}-\text{S1})p.\text{adj} = 0.643197$. Each dot represents one animal with symbols for female (circle) and male (triangle). Number of animals per region = 22. c: Confocal images of immunostained microglia (Iba1, green) and cell nuclei (Hoechst, blue) from ovariectomized C57BL/6J adult mice for each brain region with zoom-in. Scale bar: 50 μm . SD: standard deviation.



Extended Data Fig. 5 | See next page for caption.

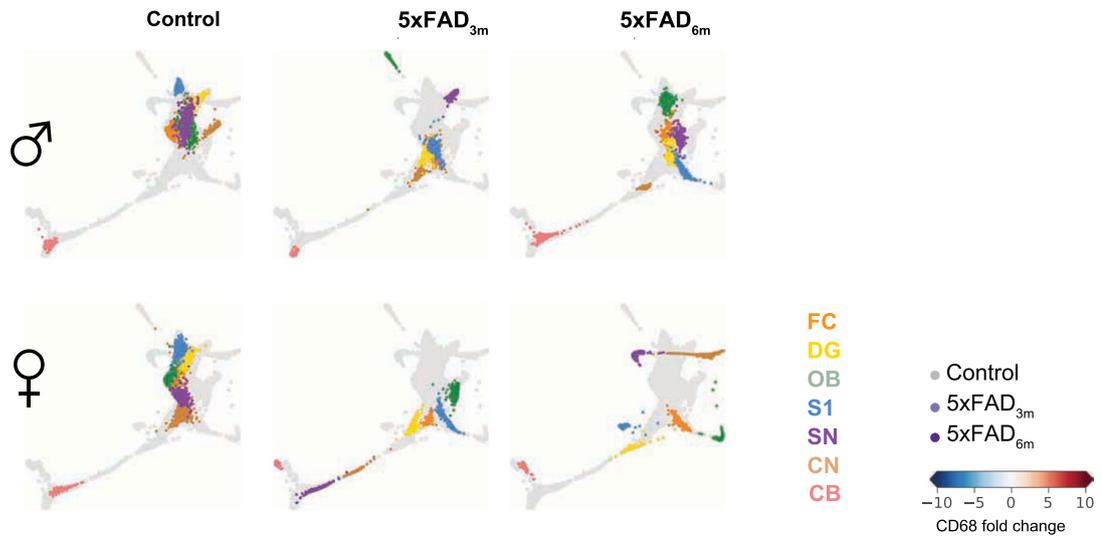
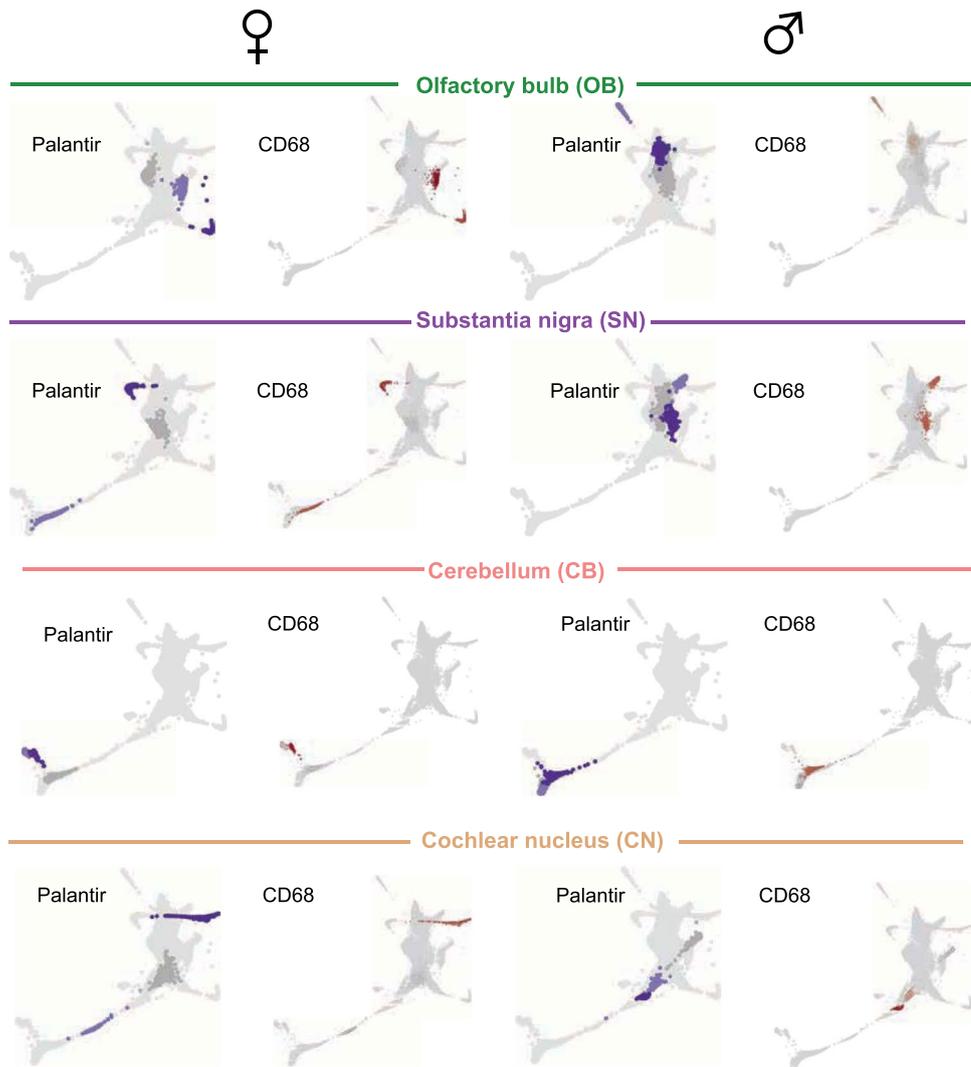
Extended Data Fig. 5 | Microglial phenotypic spectrum during postnatal development. a: Sagittal view of analyzed brain regions: olfactory bulb (OB), frontal cortex (FC), dentate gyrus (DG), somatosensory cortex (S1), substantia nigra (SN), cochlear nucleus (CN) and cerebellum (CB). **b:** Confocal images of GFP⁺ microglia (green) and cell nuclei (Hoechst, blue) from Cx3cr1^{+/GFP} mice at P7,

P15, and P22 for each brain region with zoom-in. Scale bar: 50 μm . **c:** UMAP plots of MorphOMICs-analyzed microglia from **b** for females (left) and males (right) at P7, P15, P22, and adults. Separate UMAP for each brain region and sex. Each dot represents a bootstrapped persistence image. $n_{\text{samples}} = 500$ per condition (see also Methods: *Average and bootstrapped persistence images*).



Extended Data Fig. 6 | Microglia phenotypic spectrum in the 5xFAD model of familiar Alzheimer's neurodegeneration. a: Sagittal view of analyzed brain regions: olfactory bulb (OB), frontal cortex (FC), dentate gyrus (DG), somatosensory cortex (S1), substantia nigra (SN), cochlear nucleus (CN) and cerebellum (CB). **b:** Confocal images showing immunostained microglia (Iba1, green) and cell nuclei (Hoechst, blue) from the analyzed brain regions in 5xFAD_{3m}

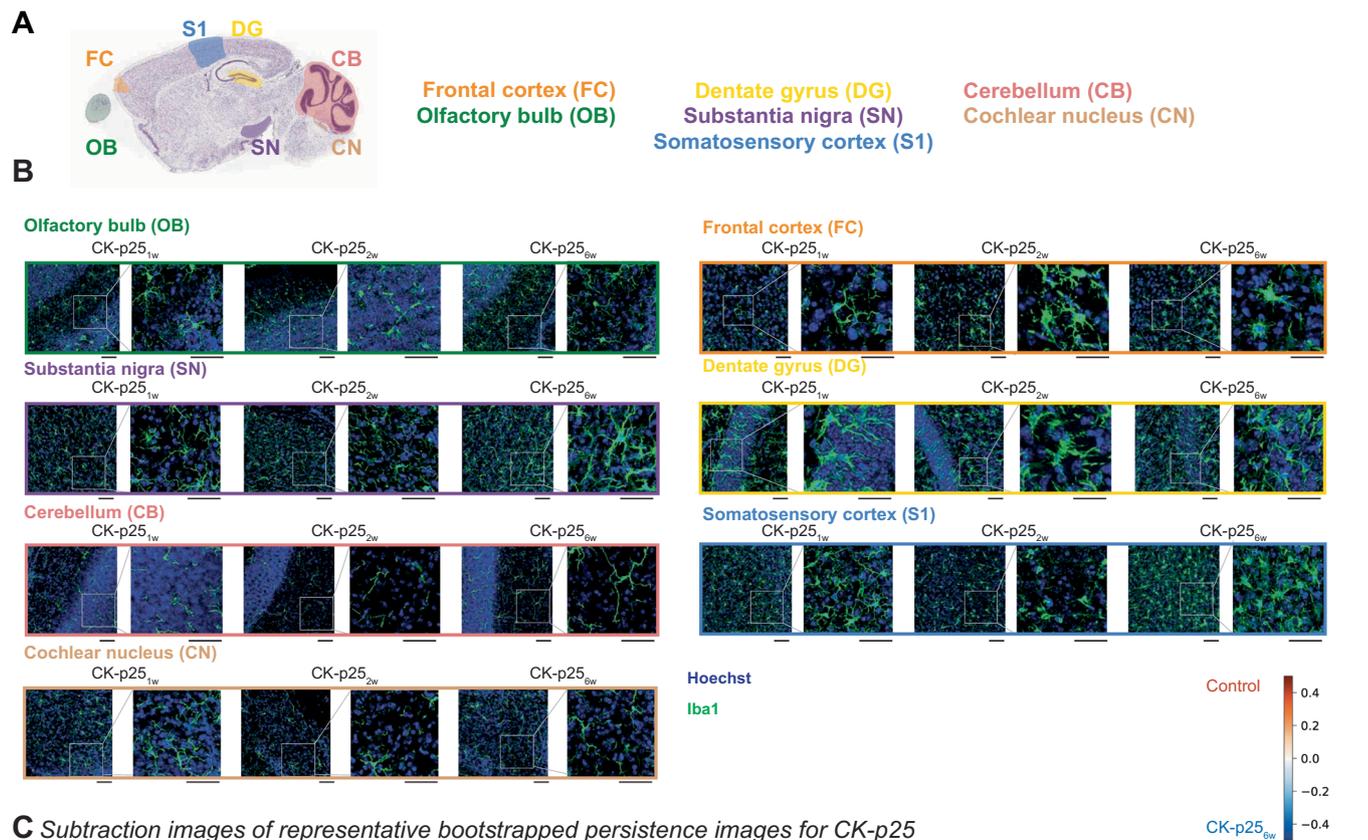
and 5xFAD_{6m} (3 and 6 months, respectively) with zoom-in. Scale bar: 50 μ m. **c:** Representative persistence images corresponding to each cluster centroid from Fig. 4b with color-coded process density. Top right corner, representative traced microglia. Subtraction image with highlighted overrepresented processes on the representative microglia.

A Morphological trajectory of microglia during degeneration in 5xFAD mice**B** Sexual dimorphism in morphological trajectory and CD68 in 5xFAD

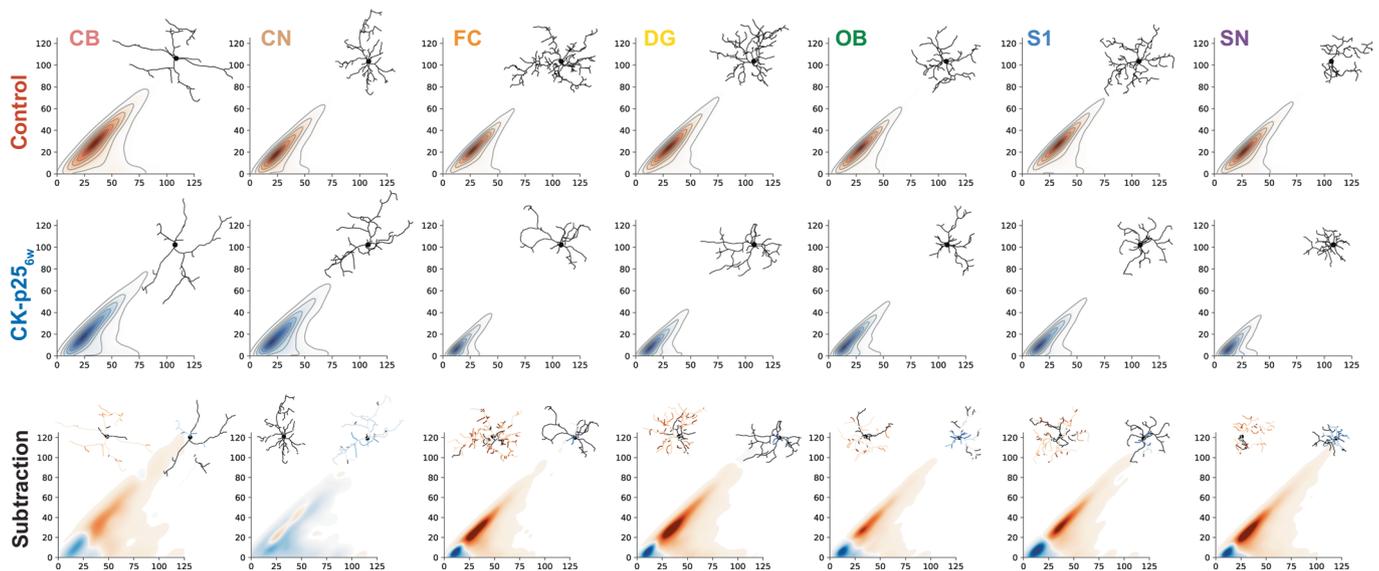
Extended Data Fig. 7 | See next page for caption.

Extended Data Fig. 7 | Sexually dimorphic microglia phenotype in 5xFAD. a: Palantir reconstruction of microglial morphological trajectory in males (top) and females (bottom). Each time-point highlighted in a separate Palantir plot. **b:** Palantir reconstruction of microglial trajectory with corresponding color-coded CD68 fold change next to it for females (left) and males (right) in control

adult, 5xFAD_{3m}, and 5xFAD_{6m} of OB, SN, CN, and CB. Fold change: blue < 0; red > 0. Olfactory bulb (OB), frontal cortex (FC), dentate gyrus (DG), somatosensory cortex (S1), substantia nigra (SN), cochlear nucleus (CN), and cerebellum (CB). $n_{\text{samples}} = 500$ per condition (see also Methods: *Average and bootstrapped persistence images*).

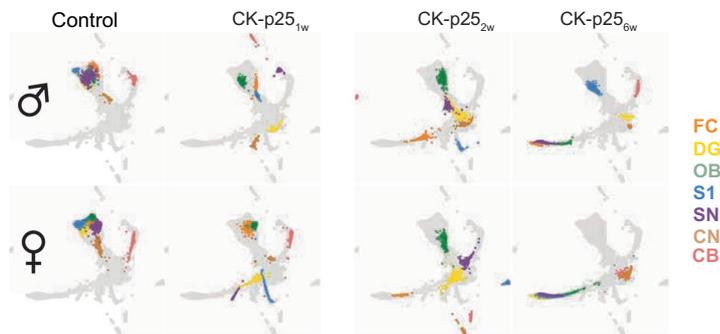
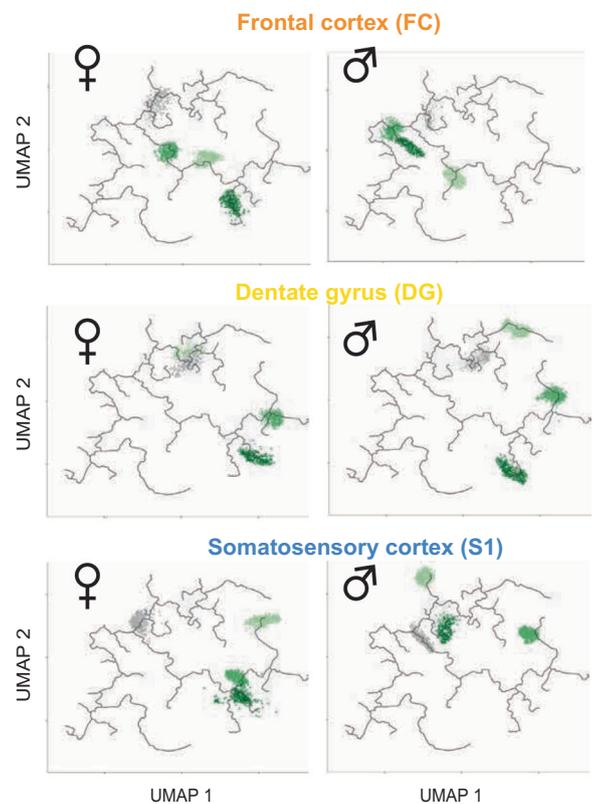
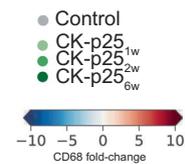
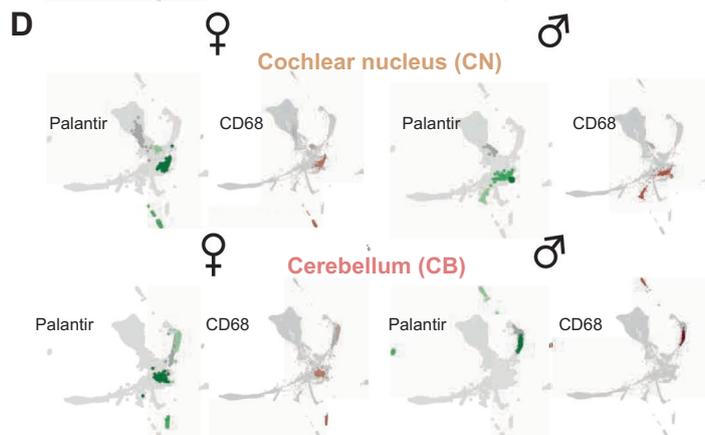
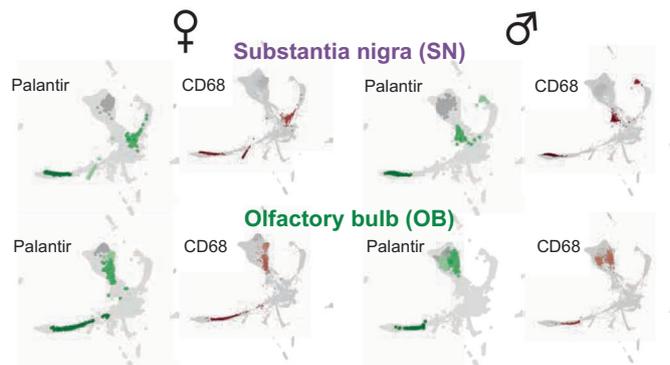


C Subtraction images of representative bootstrapped persistence images for CK-p25



Extended Data Fig. 8 | Microglia phenotypic spectrum in the CK-p25 model of sporadic neurodegeneration. **a:** Sagittal view of analyzed brain regions: olfactory bulb (OB), frontal cortex (FC), dentate gyrus (DG), somatosensory cortex (S1), substantia nigra (SN), cochlear nucleus (CN) and cerebellum (CB). **b:** Confocal images showing stained microglia (Iba1, green) and cell nuclei (Hoechst, blue) from analyzed brain regions and CK-p25_{1w}, CK-p25_{2w},

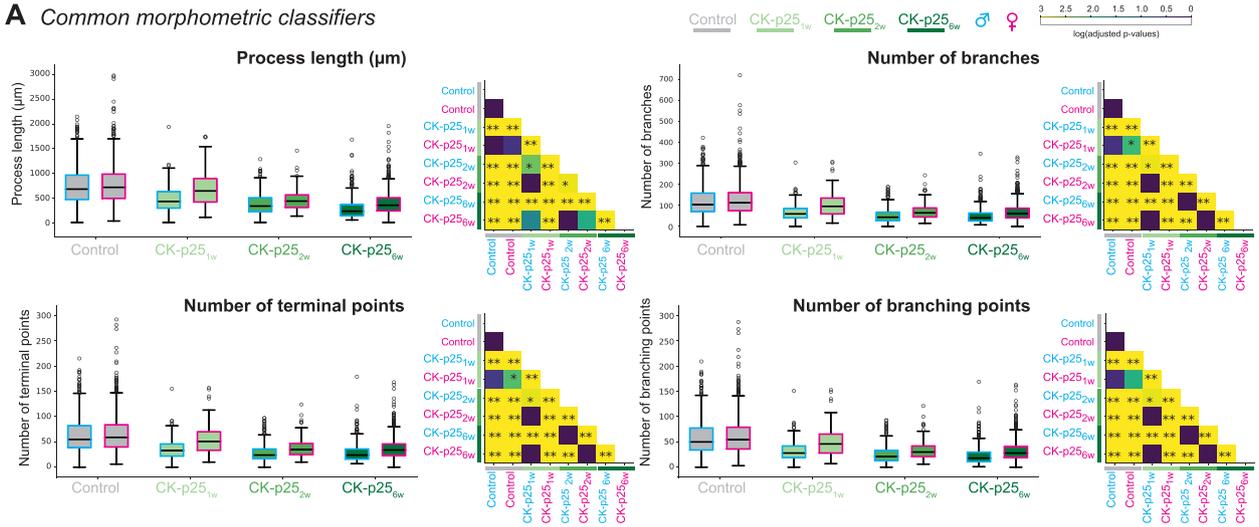
CK-p25_{6w} mice (1-, 2- and 6-weeks after doxycycline withdrawal) with zoom-in. Scale bar: 50 μ m. **c:** Representative persistence images corresponding to each cluster centroid from Fig. 5b with color-coded process density. Top right corner, representative traced microglia. Subtraction image with highlighted overrepresented processes on the representative microglia.

A Morphological trajectory of microglia in CK-p25 mice**B** Sex-specific Monocle trajectory of microglial morphology in CK-p25**C** Sexual dimorphism in morphological trajectory and CD68 in CK-p25

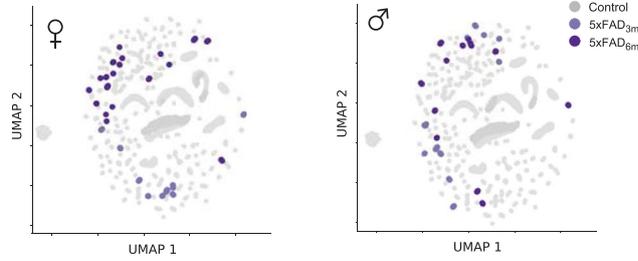
Extended Data Fig. 9 | Sexually dimorphic microglial phenotype in CK-p25. **a:** Palantir reconstruction of microglial morphological trajectory in males (top) and females (bottom) in control and CK-p25 mice. Each disease time-point highlighted in a separate Palantir plot. **b:** Monocle reconstruction of microglia trajectory of females (left) and males (right) in control, adult and CK-p25

mice FC, DG, and S1. **c-d:** Palantir reconstruction of microglia trajectory and corresponding color-coded CD68 fold-change of females (left) and males (right) for SN, OB (**c**) and CN, CB (**d**). Fold change: blue < 0; red > 0. $n_{\text{samples}} = 500$ per condition (see also Methods: *Average and bootstrapped persistence images*).

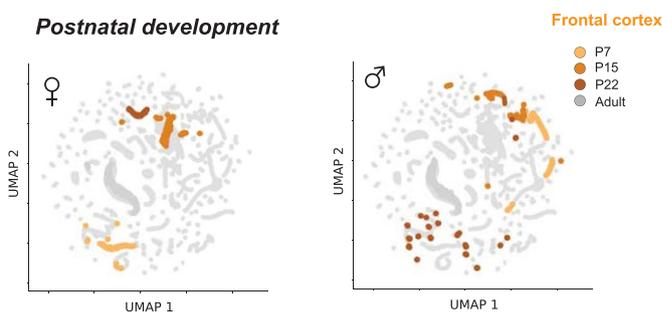
A Common morphometric classifiers



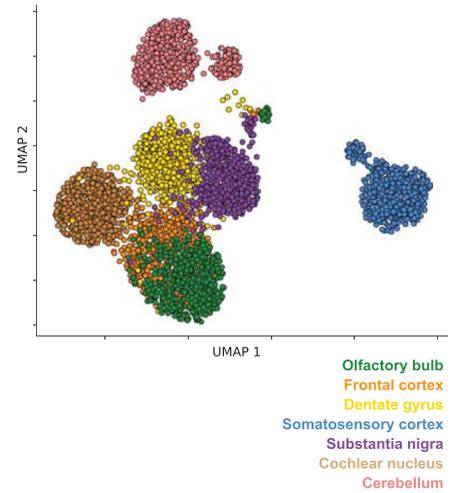
B Bootstrap application to an extended set of morphometric classifiers 5xFAD



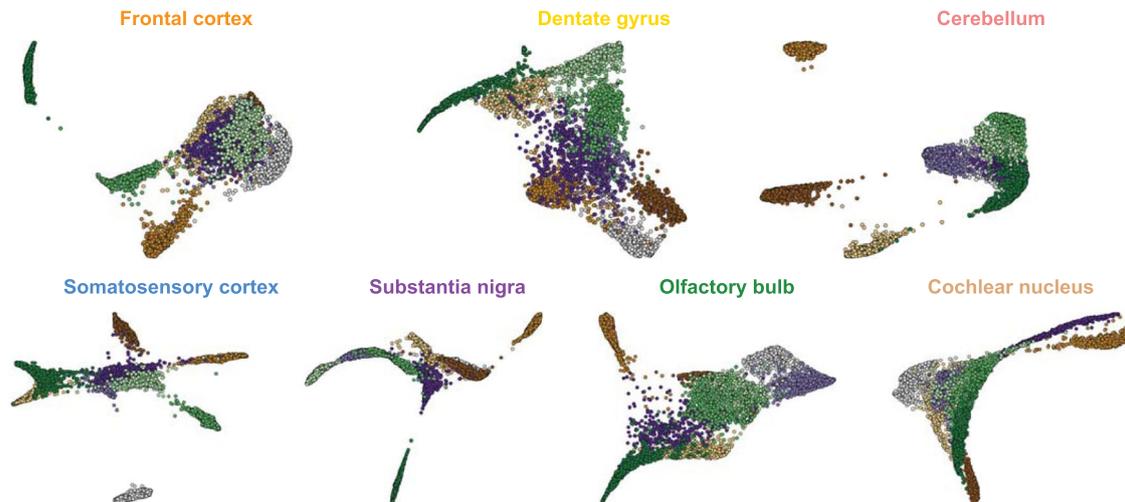
C Postnatal development



D UMAP of bootstrapped of morphometrics set



E Comparison of all-sex morphological trajectories in development and disease through all brain regions



Extended Data Fig. 10 | See next page for caption.

Extended Data Fig. 10 | Classical morphometric do not recapitulate MorphOMICs observations. a: Box plots for the selected features process length, number of branches, terminal- and branching points of control ($n_c=926$, $n_s=894$), and CK-p25_{1w} ($n_c=219$, $n_s=194$), CK-p25_{2w} ($n_c=264$, $n_s=492$), CK-p25_{6w} ($n_c=858$, $n_s=462$) mice (1-, 2- and 6-weeks after doxycycline withdrawal, respectively) in the frontal cortex (FC). For number of animals per condition and region see also Supplementary Table 5. Box denotes first and last quartile with central line indicating the median. Whiskers: range of quantities. Open circle: outliers. Next: Matrices showing color-coded p-values for the pairwise comparison of each morphometric. Kruskal-Wallis test, Bonferroni correction using Dunn's test, * $p < 0.05$, ** $p < 0.01$ (see Supplementary Table 1). **b, c:** Bootstrapped and

UMAP representations of an extended set of morphological classifiers (see Supplementary Table 3) applied to females (left) and males (right) in 5xFAD (**b**) and developmental time points (**c**) with highlighted frontal cortex (calculation without cochlear nucleus and cerebellum for simplicity). Each dot represents an averaged extended set of morphometric classifiers across 30 microglia that form the bootstrap population. **d:** Morphometric UMAP of the bootstrapped comprehensive 27 morphometrics set showing regional heterogeneity of microglia in adult healthy mice. Brain regions are color-coded. **e:** Reference atlas for each brain region represented as Palantir reconstruction containing both sexes. $n_{samples} = 300$ (**B-D**) and $n_{samples} = 200$ (**E**) per condition (see also Methods: *Average and bootstrapped persistence images*).

Reporting Summary

Nature Portfolio wishes to improve the reproducibility of the work that we publish. This form provides structure for consistency and transparency in reporting. For further information on Nature Portfolio policies, see our [Editorial Policies](#) and the [Editorial Policy Checklist](#).

Statistics

For all statistical analyses, confirm that the following items are present in the figure legend, table legend, main text, or Methods section.

n/a Confirmed

- The exact sample size (n) for each experimental group/condition, given as a discrete number and unit of measurement
- A statement on whether measurements were taken from distinct samples or whether the same sample was measured repeatedly
- The statistical test(s) used AND whether they are one- or two-sided
Only common tests should be described solely by name; describe more complex techniques in the Methods section.
- A description of all covariates tested
- A description of any assumptions or corrections, such as tests of normality and adjustment for multiple comparisons
- A full description of the statistical parameters including central tendency (e.g. means) or other basic estimates (e.g. regression coefficient) AND variation (e.g. standard deviation) or associated estimates of uncertainty (e.g. confidence intervals)
- For null hypothesis testing, the test statistic (e.g. F , t , r) with confidence intervals, effect sizes, degrees of freedom and P value noted
Give P values as exact values whenever suitable.
- For Bayesian analysis, information on the choice of priors and Markov chain Monte Carlo settings
- For hierarchical and complex designs, identification of the appropriate level for tests and full reporting of outcomes
- Estimates of effect sizes (e.g. Cohen's d , Pearson's r), indicating how they were calculated

Our web collection on [statistics for biologists](#) contains articles on many of the points above.

Software and code

Policy information about [availability of computer code](#)

Data collection

Details about obtaining 3D-microglial morphologies are outlined in the Material and Methods under the sections: Animals, Brain samples and analyzed brain regions, Ovariectomy, Transcardiac perfusion, Vibratome sections, Immunofluorescence staining, Confocal microscopy, Image processing, and Reconstruction of 3D-traced microglia.

For data collection, the following codes/software were used: Imaris Stitcher v9.3.1, Fiji 1.52e, in Imaris 9.2.v (Bitplane Imaris), ImarisReader toolbox for MATLAB (<https://github.com/PeterBeemiller/ImarisReader>), NL Morphology Converter (<http://neuroland.org>).

Data analysis

Data analysis is described in Material and Methods sections of the manuscript under the sections: Analysis of morphometric features, Topological morphology descriptor (TMD), Average and bootstrapped persistence images, TMD distance, Hierarchical clustering, Dimensionality reduction, tSNE, Pseudotemporal ordering, Palantir, Monocle, Stable ranks analysis, and Bootstrapped morphometric features. All the MorphOMICS codes used are available through a GitHub library: <https://git.ist.ac.at/rcubero/morphomics>.

On top of the MorphOMICS codes, the following codes/software were used: L-measure (<http://cng.gmu.edu:8080/Lm/>), NeuroM Python toolkit (<https://github.com/BlueBrain/NeuroM>), cluster.hierarchy.linkage from SciPy v1.6.2, sklearn.svm.SVC from sklearn (<https://scikit-learn.org/stable/>), scipy.stats (v1.6.2) and scikit-posthocs (v0.6.7) and R (v3.4.4).

For manuscripts utilizing custom algorithms or software that are central to the research but not yet described in published literature, software must be made available to editors and reviewers. We strongly encourage code deposition in a community repository (e.g. GitHub). See the Nature Portfolio [guidelines for submitting code & software](#) for further information.

Data

Policy information about [availability of data](#)

All manuscripts must include a [data availability statement](#). This statement should provide the following information, where applicable:

- Accession codes, unique identifiers, or web links for publicly available datasets
- A description of any restrictions on data availability
- For clinical datasets or third party data, please ensure that the statement adheres to our [policy](#)

All the .swc files are available at the NeuroMorpho.org repository in the Siegert archive under the link: <https://neuromorpho.org/KeywordResult.jsp?keywords=%22siegert%22>.

We have also used the Allen Developing Mouse Brain Atlas - Sagittal atlas to illustrate the locations of brain regions-of-interest. The image was taken from <https://atlas.brain-map.org/atlas?atlas=2#atlas=2&plate=100883770&structure=549&x=7799.7333984375&y=4022.93359375&zoom=-3&resolution=16.75&z=5>.

Field-specific reporting

Please select the one below that is the best fit for your research. If you are not sure, read the appropriate sections before making your selection.

Life sciences Behavioural & social sciences Ecological, evolutionary & environmental sciences

For a reference copy of the document with all sections, see [nature.com/documents/nr-reporting-summary-flat.pdf](https://www.nature.com/documents/nr-reporting-summary-flat.pdf)

Life sciences study design

All studies must disclose on these points even when the disclosure is negative.

Sample size	No statistical methods were used to pre-determine sample sizes but our sample sizes are similar to those reported in previous publications (Morrison et. al., 2013, Heindl et. al., 2018, Kongsui et. al., 2014, Tan et. al., 2019, Stratoulis et. al., 2019, Bachstetter et. al., 2015, Salamanca et. al., 2019, Del Mar Fernandez-Arjona, et. al., 2017).
Data exclusions	1.) After the tracing, we manually removed cells that were sitting at the border of the image and were only partially traced so that these cells would not be analyzed. 2.) Morphologies with only one branch (and consequently, one topological bar) were excluded from the analysis. No other exclusion criteria were imposed.
Replication	For each condition [C57BL/6J adult mice (8-12 weeks (=adult), ovariectomized); Cx3cr1GFP/- mice at postnatal time points P7, P15, P21; 5xFAD mice after 3 and 6 months; and CK-p25 mice 1, 2, and 6 weeks after doxycycline withdrawal], we analyzed seven brain regions [OB, FC, S1, DG, SN, CN, CB]. Each condition was analyzed for both sexes [male/female] with at least biological triplicates. A breakdown of animals used per condition is detailed in Extended Data Table 5. The total number of traced microglia per condition divided by sex is shown in Extended Data Table 1. All microglia reconstructed across animals (after exclusion condition, see above) were pooled together. Within each condition, no animal-specific differences in morphologies were detected (Extended Data Figure 1E), indicating successful replication.
Randomization	For every experimental group (as determined using the genotype and age of the mouse), we randomly selected the same number of female and male mice based on the mouse IDs, across different litters. All reconstructed microglia morphologies (after imposing exclusion criteria) were pooled together. In the MorphOMiCs implementation, bootstrapped samples were obtained from random selection of microglia conditioned on group labels, which provides further data randomization.
Blinding	For the analysis, we pre-selected the brain regions to be analyzed in this study (see section "Brain samples and analyzed brain regions"). For each brain region, we obtained a 2x2 tile covering an approximate area of 0.1 mm ² and kept the position consistent between animals. Over 330 images were collected from three independent scientists over the course of three years. The data collection of microglia was performed with a semi-automated reconstruction over this tile eliminating the need of a blinded sampling approach. All microglia within the tile were 3D-reconstructed. Microglia that were sitting at the border of the image and were only partially traced were excluded from the data analysis. No other exclusion has been performed. The dataset was then converted into individual skeletons that were provided to a non-biologist, who performed the data analysis based on the group labels but without knowing the meaning of the labels. Further blinding would not be feasible as the overall phenotypic differences of the brain during development and disease prevent efficient blinding.

Behavioural & social sciences study design

All studies must disclose on these points even when the disclosure is negative.

Study description	Briefly describe the study type including whether data are quantitative, qualitative, or mixed-methods (e.g. qualitative cross-sectional, quantitative experimental, mixed-methods case study).
-------------------	---

Research sample	State the research sample (e.g. Harvard university undergraduates, villagers in rural India) and provide relevant demographic information (e.g. age, sex) and indicate whether the sample is representative. Provide a rationale for the study sample chosen. For studies involving existing datasets, please describe the dataset and source.
Sampling strategy	Describe the sampling procedure (e.g. random, snowball, stratified, convenience). Describe the statistical methods that were used to predetermine sample size OR if no sample-size calculation was performed, describe how sample sizes were chosen and provide a rationale for why these sample sizes are sufficient. For qualitative data, please indicate whether data saturation was considered, and what criteria were used to decide that no further sampling was needed.
Data collection	Provide details about the data collection procedure, including the instruments or devices used to record the data (e.g. pen and paper, computer, eye tracker, video or audio equipment) whether anyone was present besides the participant(s) and the researcher, and whether the researcher was blind to experimental condition and/or the study hypothesis during data collection.
Timing	Indicate the start and stop dates of data collection. If there is a gap between collection periods, state the dates for each sample cohort.
Data exclusions	If no data were excluded from the analyses, state so OR if data were excluded, provide the exact number of exclusions and the rationale behind them, indicating whether exclusion criteria were pre-established.
Non-participation	State how many participants dropped out/declined participation and the reason(s) given OR provide response rate OR state that no participants dropped out/declined participation.
Randomization	If participants were not allocated into experimental groups, state so OR describe how participants were allocated to groups, and if allocation was not random, describe how covariates were controlled.

Ecological, evolutionary & environmental sciences study design

All studies must disclose on these points even when the disclosure is negative.

Study description	Briefly describe the study. For quantitative data include treatment factors and interactions, design structure (e.g. factorial, nested, hierarchical), nature and number of experimental units and replicates.
Research sample	Describe the research sample (e.g. a group of tagged <i>Passer domesticus</i> , all <i>Stenocereus thurberi</i> within Organ Pipe Cactus National Monument), and provide a rationale for the sample choice. When relevant, describe the organism taxa, source, sex, age range and any manipulations. State what population the sample is meant to represent when applicable. For studies involving existing datasets, describe the data and its source.
Sampling strategy	Note the sampling procedure. Describe the statistical methods that were used to predetermine sample size OR if no sample-size calculation was performed, describe how sample sizes were chosen and provide a rationale for why these sample sizes are sufficient.
Data collection	Describe the data collection procedure, including who recorded the data and how.
Timing and spatial scale	Indicate the start and stop dates of data collection, noting the frequency and periodicity of sampling and providing a rationale for these choices. If there is a gap between collection periods, state the dates for each sample cohort. Specify the spatial scale from which the data are taken
Data exclusions	If no data were excluded from the analyses, state so OR if data were excluded, describe the exclusions and the rationale behind them, indicating whether exclusion criteria were pre-established.
Reproducibility	Describe the measures taken to verify the reproducibility of experimental findings. For each experiment, note whether any attempts to repeat the experiment failed OR state that all attempts to repeat the experiment were successful.
Randomization	Describe how samples/organisms/participants were allocated into groups. If allocation was not random, describe how covariates were controlled. If this is not relevant to your study, explain why.
Blinding	Describe the extent of blinding used during data acquisition and analysis. If blinding was not possible, describe why OR explain why blinding was not relevant to your study.
Did the study involve field work?	<input type="checkbox"/> Yes <input type="checkbox"/> No

Field work, collection and transport

Field conditions	Describe the study conditions for field work, providing relevant parameters (e.g. temperature, rainfall).
Location	State the location of the sampling or experiment, providing relevant parameters (e.g. latitude and longitude, elevation, water depth).
Access & import/export	Describe the efforts you have made to access habitats and to collect and import/export your samples in a responsible manner and in compliance with local, national and international laws, noting any permits that were obtained (give the name of the issuing authority, the date of issue, and any identifying information).
Disturbance	Describe any disturbance caused by the study and how it was minimized.

Reporting for specific materials, systems and methods

We require information from authors about some types of materials, experimental systems and methods used in many studies. Here, indicate whether each material, system or method listed is relevant to your study. If you are not sure if a list item applies to your research, read the appropriate section before selecting a response.

Materials & experimental systems

n/a	Involvement in the study
<input type="checkbox"/>	<input checked="" type="checkbox"/> Antibodies
<input checked="" type="checkbox"/>	<input type="checkbox"/> Eukaryotic cell lines
<input checked="" type="checkbox"/>	<input type="checkbox"/> Palaeontology and archaeology
<input type="checkbox"/>	<input checked="" type="checkbox"/> Animals and other organisms
<input checked="" type="checkbox"/>	<input type="checkbox"/> Human research participants
<input checked="" type="checkbox"/>	<input type="checkbox"/> Clinical data
<input checked="" type="checkbox"/>	<input type="checkbox"/> Dual use research of concern

Methods

n/a	Involvement in the study
<input checked="" type="checkbox"/>	<input type="checkbox"/> ChIP-seq
<input checked="" type="checkbox"/>	<input type="checkbox"/> Flow cytometry
<input checked="" type="checkbox"/>	<input type="checkbox"/> MRI-based neuroimaging

Antibodies

Antibodies used

The following primary antibodies were used: rat α -CD68 (AbD Serotec, Cat#MCA1957, clone FA-11, Lot 1807); goat α -Iba1 (Abcam, ab5076, Lot FR3288145-1); rabbit anti-Iba1 (GeneTex, Cat#GTX100042, Lot 41556). The secondary antibodies raised in goat or donkey were purchased from Thermo Fisher Scientific (Alexa Fluor 488 goat anti-rabbit IgG #A11034, Alexa Fluor 647 goat anti-rat IgG #21247, 1:2000).

Validation

All listed antibodies are commercially available. The same antibodies and Lot have been successfully used in a recently peer-reviewed study (Venturino et al., Cell Rep. 2021 Jul 6;36(1):109313. doi: 10.1016/j.celrep.2021.109313).

Animals and other organisms

Policy information about [studies involving animals](#); [ARRIVE guidelines](#) recommended for reporting animal research

Laboratory animals

IST Austria: C57BL/6J (Cat#000664) and B6.129P-Cx3cr1tm1Litt/J (Cat#005582, named here Cx3cr1GFP^{-/-}, only heterozygous mice were used) were purchased from The Jackson Laboratories.
MIT: 5xFAD and CK-p25 mice were obtained from the Tsai lab at MIT. Tg(APPswF1on, PSEN1*^{M146L}*^{L286V})6799Vas/Mmjax, Stock No: 34840-JAX) were obtained from Jackson laboratory. CK-p25 mice were generated by breeding CaMKII α promoter-tTA mice (CK controls) (B6;CBA-Tg(Camk2a-tTA)1Mmay/J, Jackson Laboratory, Stock No: 003010) with tetO-CDK5R1/GFP mice (C57BL/6-Tg(tetO-CDK5R1/GFP)337Lht/J, Jackson Laboratory, Stock No: 005706). CK-p25 mice and their CK control littermates were conceived and raised in the presence of doxycycline-containing food to repress p25 transgene expression. To induce p25 transgene expression, mice were fed a normal rodent diet. p25 transgene expression was induced in adult mice at the age of 3 months. Animal from both sexes were used, as indicated in the Methods.

Housing conditions: All animals are housed in groups of three to five in commercially available, individually ventilated cages (IVCs) made of Polysulfon under precisely defined standard laboratory conditions (room temperature 22 \pm 1 $^{\circ}$ C; relative humidity 55 \pm 10 %; photoperiod 12L:12D), supplied with standard diet (rat/mouse maintenance diet (V1534-300) or mouse breeding diet (V1124-300), sniff Spezialitäten GmbH) and autoclaved water ad libitum.

Age: Adult (C57BL/6J) control and ovariectomized mice were 2-3 months old at time of perfusion. Cx3cr1GFP^{-/-} mice were sampled at postnatal days 7, 15, and 22. 5xFAD mice were collected at 3 and 6 months. After induction of p25 expression at age of 3 months, CK-p25 mice were collected after 1, 2 and 6 weeks. C57BL/6J mice were 2-3 months old upon administration of the anesthetic cocktail ketamine-xylazine-acepromazine (KXA).

Wild animals

No wild animals were used in this study.

Field-collected samples

No field-collected samples were used in this study.

Ethics oversight

IST Austria: All animal procedures are approved by the Bundesministerium für Wissenschaft, Forschung und Wirtschaft (bmwfw) Tierversuchsgesetz 2012, BGBl. I Nr. 114/2012, idF BGBl. I Nr. 31/2018 under the numbers 66.018/0005-WF/V/3b/2016, 66.018/0010-WF/V/3b/2017, 66.018/0025-WF/V/3b/2017, 66.018/0001_V/3b/2019, 2020-0.272.234.
MIT: All animal work was approved by the Committee for Animal Care of the Division of Comparative Medicine at the Massachusetts Institute of Technology.

Note that full information on the approval of the study protocol must also be provided in the manuscript.